A new approach for processing X-ray data for detecting mini-halos in galaxy clusters

by

Zareef Jafar
17301178
Armin Nahar Mim
16301067
Sworna Roy
19301279

A thesis submitted to the Department of Computer Science and Engineering
in partial fulfillment of the requirements for the degree of
B.Sc. in Computer Science

Department of Computer Science and Engineering
Brac University
June 2021

Declaration

It is hereby declared that

1. The thesis submitted is my/our own original work while completing degree at Brac University.

2. The thesis does not contain material previously published or written by a third party, except where this is appropriately cited through full and accurate referencing.

3. The thesis does not contain material which has been accepted, or submitted, for any other degree or diploma at a university or other institution.

4. We have acknowledged all main sources of help.

Student's Full Name & Signature:

Zareef Jafar
17301178

Armin Nahar Mim
16301067

Sworna roy
19301279

Approval

The thesis/project titled "A new approach for processing X-ray data for detecting mini-halos in galaxy clusters" submitted by

1. Zareef Jafar (17301178)
2. Armin Nahar Mim (16301067)
3. Sworna Roy (19301279)

Of Spring, 2021 has been accepted as satisfactory in partial fulfillment of the requirement for the degree of B.Sc. in Computer Science on June 02, 2021.

Examining Committee:

Supervisor:
(Member)

Dr. Amitabha Chakrabarty
Associate Professor
Department of Computer Science and Engineering
BRAC University

Thesis Coordinator:
(Member)

Dr. Md. Golam Rabiul Alam
Associate Professor
Department of Computer Science and Engineering
Brac University

Head of Department:
(Chair)

Dr. Sadia Hamid Kazi
Chairperson and Associate Professor
Department of Computer Science and Engineering
Brac University

Abstract

Galaxy clusters, which may contain hundreds or thousands of galaxies, are the biggest gravitationally bound objects in the universe. These clusters are filled with heated X-ray emitting plasma. Radio mini-halos are radio sources which are found in some cool-core non-major merging galaxy clusters and study of these mini halos helped scientists to unveil many other mysteries of how the universe works. Till now 23 such galaxy clusters have been found, many with confirmed minihalo and some with potential mini-halos. Even a few years ago observational data of this kind of astronomical observations were available only to the astronomical communities and specific research institutions. As more and more data is publicly available it made a way for Amateur astronomers and students who want to work with real data. In our work we use such publicly accessible X-ray data of these galaxy clusters from Chandra X-ray Observatory for determining the cold front which ultimately will give us the location of these mini halos. The main goal of our thesis is to develop a workflow using some open-source Astro data processing packages and including our own python script for such purpose. These software tools include CIAO, ClusterPyXT pipeline, conda and our own python script. This workflow includes setting up the proper software environments, list of packages needed, rules for choosing different input parameters for downloading as well as processing data successfully and some sources to compare the generated output. From start to end this process can be successfully run on any moderate modern desktop computer.

Keywords: Galaxy clusters, X-ray, mini-halos, Cold Front, ClusterPyXT, CIAO, python

Dedication

We would like to dedicate this thesis to our loving parents, supervisor, co-supervisor and everyone out there who helped us throughout our work.

Acknowledgement

Firstly, we are grateful to our supervisor Dr. Amitabha Chakrabarty for letting us work on such a topic and for his generous advice till the end. His thoughtful and visionary solutions helped us stay on track.
Secondly, we are very lucky to have Dr. Khan Asad as our co-supervisor from the very beginning with his humble assistance and handful of contributions whenever we needed it. We are grateful to Dr.Tibra Ali for making it possible.
We also like to show our gratitude towards Jean-Paul Breuer for introducing us to his software tool and his advice about using it which we are planning to use in the future. Moreover, thanks to some advice from Dr. Grant Tremblay we were able to fix some issues in our processing promptly.

Table of Contents

List of Figures

List of Tables

Nomenclature

The next list describes several symbols & abbreviation that will be later used within the body of the document

ne Electron

ni ion number density

rc Radius of the X-ray Nucleus

α Alpha

β Beta

$_0$ density of the Central Gas

λ Lamda

ρ Rho

ACB Adaptive Circular Binning

ACIS Advanced CCD Imaging Spectrometer

CCD Charge-Coupled Device

CIAO Chandra Interactive Analysis of Observations

DM Dark Matter

FITS Flexible Image Transport System

g_{ff} Gaunt Factor

Gyr Gigayear

HEASARC High Energy Astrophysics Science Archive Research Center

keV Kilo Electron Volts

Kpc kiloparsecs

MH Mini Halos

rj Jump radii

WVT Wavelet Transform

Chapter 1

Introduction

The application of phenomenal evolution in computer science has no bound. Thus, with the hope of doing something significant we are looking forward to using our capability according to our present knowledge and understanding on such a topic, where we are thinking of developing a method including a step by step guide to process X-ray data to detect the location of mini-halos from galaxy clusters by generating 'Density and Brightness Map'. We also are looking forward to creating a python script for the final result generation by the distinct completion phase of our work.

1.1 Background

In the era of large-scale astronomical surveys, methods to investigate data, and especially to classify astronomical objects, become more and more critical. We see more and more tools, techniques, and implications of Computer Science, Data Science, ML, and Statistical in real - time astronomy. The format of these astronomical data is different from other data used in the field of data analysis. So, astronomers need to develop different tools for different astronomical applications. Most of the data are from different kinds of telescopes and observatories. Other telescopes detect other electromagnetic waves, from radio waves to gamma rays. The tools and packages are developed in a wide variety of platforms and not easy to use. Moreover, most of the methods and tools used in astronomy are not publicly available and well-documented.

The space contains a number of extremely gigantic dense creations such as galaxy clusters. So, it is one of the most studied astronomical objects in the field of space science. The phenomenon called mini-halo is one of the recent objects of study for these galaxy clusters. As more and more data is being collected from different telescopes of galaxy clusters, methods are being developed for detecting mini-halos of these galaxy clusters and X-ray data from . The goal of our thesis is to develop a method and a step-to-step guide to process X-ray data to detect the location of mini-halos from galaxy clusters. All the tools we are using are publicly available, and in the end, we also have used our python script for the final result generation, which we uploaded on GitHub. However, users need some basic knowledge of bash and different astronomical parameters for tweaking some values. We also provided some guides and online tools to help the user choose these values for his desired galaxy clusters. To implement this user does not need any server-level computational power.

1.2 Research Problem

There is a considerable possibility that in-depth knowledge on the properties of the hot gas and galaxy clusters may reveal information about their origins. Clusters emerge in order of massive structural properties by assembling distinct galaxies, sometimes other clusters.

We know there are only 25 galaxy clusters with mini-halos, but research is undergoing to confirm many of their existence. So, this field of astronomy is relatively new. As mentioned before, the data and many tools for processing them are very hard to avail to the normal users, often interested students fail in working and exploring this territory. We find this as a scope of working and building something user friendly with the accessible resources for the interested people.

1.3 Objective

The main objective of our thesis is to build a method and a workflow specially designed to detect mini-halos using some open-source tools. As a result any advanced user can manipulate them according to their need. Because of the availability of data and tools we have used, anyone can follow our analysis structure and contribute to this enormous field of computational astronomy, which will also help the developers of these astronomical software packages to extend their capability day by day.

Users will only need basic bash scripting and python knowledge to successfully implement our method for detecting min-halo in his/her desired galaxy cluster. For this reason, the scope of our thesis is only limited to X-ray processing. Confirming mini-halo also needs radio data which needs several days for processing even in supercomputers.

Chapter 2

Related Work and Literature Review

In this part of our paper, we are going to include all the related work we need to have an insight into understanding the purpose of our work and continue our work with proper knowledge of its related area.

2.1 Galaxy Cluster

Galaxy clusters are one of the largest formations of galaxies, bounded by gravity. Galaxy clusters are more than just a collection of galaxies. Each galaxy cluster consists of approximately 85% of dark matter, 10% of ICM, and 5% of galaxies[1]. In the past years, knowledge of galaxy clusters was vague. X-ray astronomy helped in acquiring circumstantial information of galaxy clusters day by day. They are relatively separated signifiers for early phase transformation, expanding on the Hubble timescale from the Cosmic Web and a good territory for researching physical plasma processes, also the interactions of super-massive black holes with the surrounding cluster plasma. Tremendous progress has occurred in the knowledge of galaxy clusters in the last decade, from their formation and evolution to their role in the radial distance creation of the Universe. These breakthroughs have been facilitated by tremendous advancements in theoretical and mathematical simulation accompanying a plethora of new data generated by multi-wavelength observations of the Universe.

2.2 ICM

Intra Cluster Medium or ICM is a kind of infrequent and extremely heated plasma with a weak magnetic field but rich in metals and ionic energy. The ICM makes up the majority of ideal baryons, mostly ionized gases such as hydrogen and helium[28]. Heavy elements like iron are contained in this plasma. The gravitational field of galaxy clusters makes the supernovae releasing metal-enriched gas, and the gases stay gravitationally bound as ICM is a part of the galaxy cluster. ICM is helpful in making a historical interpretation of the development of entities of a galaxy. The average quantity of heavier elements corresponding to hydrogen ranges from a third to a half of the value in the sun. Because of having such a high tempera-

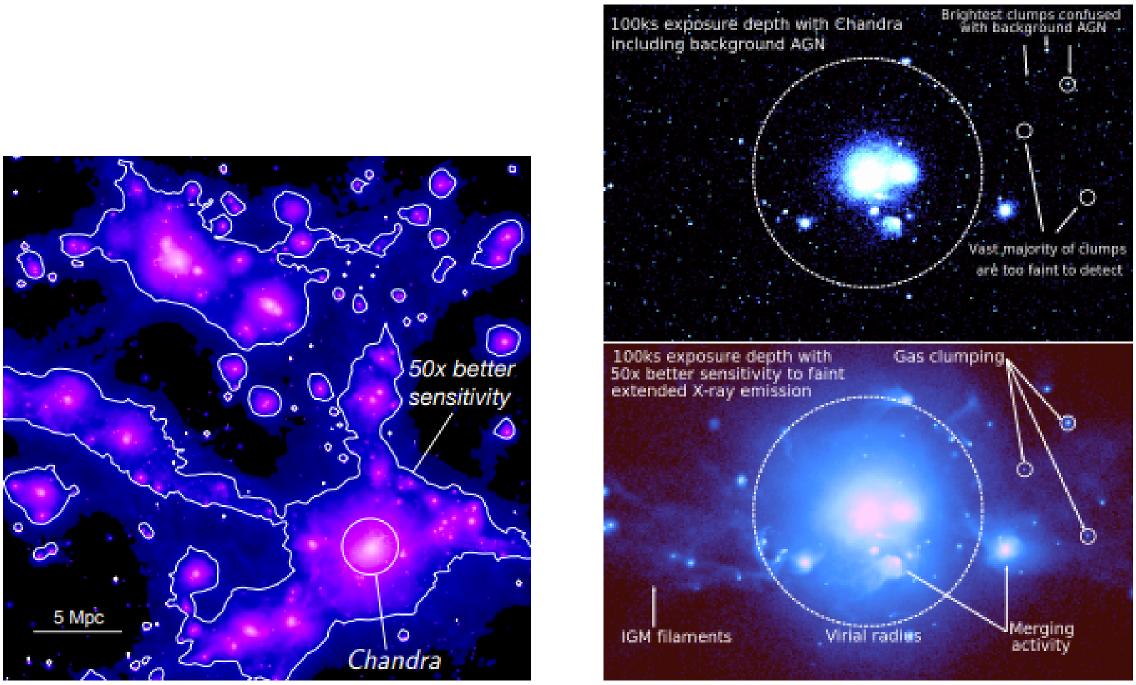

Figure 2.1: Left: A hydrodynamical cosmological simulation of large-scale structure formation reveals that galaxy clusters exist at IGM filament nodes[21].Only the core regions of clusters can be thoroughly investigated using Chandra and XMM-Newton (inner white circle). To keep developing a massive structure in its totality (outer white contours), susceptibility to low surface brightness expanded exposure must be improved by a factor of 50. Right: A simulated X-ray mosaic of the RomulusC cluster[40], a low mass (1014 M) cluster at, contrasting 100ks deep Chandra (top) and AXIS/Lynx (bottom) coverage (bottom). The cosmic X-ray history is represented by point sources in the mock Chandra simulation. We can only see the brightest X-ray emission in cluster cores due to the high background and limited collecting regions of existing X-ray telescopes. The majority of the ICM outside the virial radius (dashed white circle) and the IGM filaments that bind clusters reside concealed from view.

ture,the gas of ICM produces X-ray and synchrotron radiation through the emission lines of the heavy metals and bremsstrahlung process. Thermal Bremsstrahlung, one of the main mechanisms, generates X-ray emission in ICM[28]. Bremsstrahlung is an electromagnetic emission phenomenon occurring by deceleration of the rest energies of the ionized particles within a small range compared to their large energies. If an e is deflected by a positive charge at a near flyby, Bremsstrahlung radiation is produced. The thermal transformation inside electron configuration (2s to 1s) of hydrogen and helium ions inside the ICM is an exception to bound-bound transitions. The movement is anomalous, which means it doesn't follow angular momentum sustainability instead is a two-photon process[3]. This "two-photon radiation" requires a distribution function of the energy balancing of the two electrons and corresponds to continuous radiation. Synchrotron radiation is the primary radio frequency emission process in the ICM. When each electron radiates spontaneously, the total emission from the set of such relativistic electrons is only the sum of all the distinct contributions, depending on the electron's energy supply. The spectra type of synchrotron emission is complex and can exceed frequencies that are many times as often as the gyration frequency.

2.3 Mini-Halos(MH)

A faint scattered region surrounding the galaxy clusters, generated by radio emission, is familiar as Mini-halos. Up to now, approximately thirty mini-halos have been found. Electrons inside ionized gases emit radio and X-ray, and mini-halos are produced as the consequences. The radio and X-ray emitting electrons supposedly emerged from the energy around a galactic nucleus of a supermassive black hole. Radiohalos have low surface brightness and are extended throughout the cluster volume and the standard size is around 1 Mpc. Their formation is quite regular and their radio emission is unpolarized up to a level of a few percent. On the contrary MH are a smaller version of giant radio haloes.

2.4 Dark Matter(DM)

During the late 19th century, some just as amazing facts about the creation were made, including that traditional baryonic matter[33]. Both protons and neutrons are present at the same time in this material, which means it is neither the fundamental form of subatomic particles nor a combination of protons and neutrons. As strange as it may seem, a substance we have yet to identify called dark matter is present in our existence. In the vast majority of cases, it is around five times more massive than an ordinary matter. A thorough comprehension of dark matter necessitates the application of many fields of physics and astronomy[33]. Many other fields of physics are involved, making dark matter research a complex and collaborative territory. Moreover, One of the benefits of recent technological advancements has been the number of ground and spacecraft observations, which has increased the complexity and relevance of the discipline. ; the age of "precision cosmology" has entere[33].

2.5 Literature Review

To subtly assimilate all related terms We have gone through plenty of related works. The content for discussion of those works was to examine faint minihalos, X-ray emission from galaxy clusters, thermal Bremsstrahlung radiation, dark matter of our universe, and various terms related to astronomy using different approaches, algorithms, software, and so on. Among those works we selected a few papers to decide exactly what we are going to do in our thesis.

In paper[32] K. M. B. Asad and his mates have come up with an idea, where they chose to undertake a research of the emergence of CF and Radio Mini-halos in galaxy clusters, and for this they examined and compared the Chandra X-ray data of six host clusters' radio data[32]. Chandra X-ray data of the selected clusters have been studied here to attain their goal. They have generated X-ray images, computed surface maps, temperature maps, and the number of the coefficients of the MSVST curve. With the help of different multi-scale analyses, they have decomposed the images into different necessary resolutions. The MH radio contours were superposed on the maps after deciding the CF positions. Inevitable type of Wavelet transforms has been also used here to split targeted data into different scale components. The Curvelet transforms, another multiscale analysis, has been used here as the supplement of the Wavelet Transforms method. They tested the hypothesis that the same gas sloshing mechanism would generate CFs and MHs in the ICM X-ray photograph, you can easily detect cold front lines to find brightness borders. They were able to detect two edges in almost all clusters by following the sudden shift in color of brightness maps. We know that in regions with sharp discontinuities contour lines are compressed. From these compressions, they may deduce the location of the CF. A comparison of the brightness and temperature maps shows the rise in temperature that corresponds to a decrease in brightness around the rims. Researchers analyzed x-ray observations of six mini-halos radio galaxy clusters and found two cold fronts in each. In certain clusters, the MHs are also spatially linked to the gas sloshing spiral structure. They finally state that their prepared result by filtering, sampling, and analyzing the data agree with the MG08 analysis. The turbulence caused by the sloshing ICM gas could reaccelerate the relativistic electrons in the MHs.

In paper [39] Simona Giacintucci and her mate intended to show, diffuse unidentified synchrotron origins in cool core cells of certain galaxy clusters are radio minihalos. The minihalo radio luminosity is not strongly related to total cluster mass. Their findings indicate that while it is important to explain the origins of minihalos, it is also important to point out the many similarities between heated plasma and cold clusters. In order to extend the minihalos review, they apply GMRT and VLA data. The survey is then 23, the highest to date sample. The author assumes that the light source could be linked to the sloshing of core gases and the acceleration of the electron due to turbulence in the core gas. They assume that emissions are generally limited by concentrated cold fronts. They say new mini halos were found by them named A2667, A907, and PSZ1 G139.61+24.20.In addition, they have reviewed the VLA $1 \cdot 4$ GHz Archive observations from seven Minihalos Cluster candidates previously identified by astronomers [39]. The association between Minihalo energy and the X-ray-bolometric luminosity throughout the cool core has been relatively high ($r < 60kpcs$) has been stated. They find that this complements their previous finding (G17) that most, not each of them but massive clusters are present in the cool center.

In [38] B. Alden and his mates explain the usage of ClusterPyXT in-depth in this paper. Glimpses into the physical characteristics of a galaxy cluster may be obtained through spectral X-ray temperature maps. According to their work, the data output extracted by ClusterPyXT may contribute to a greater understanding of the actual physics behind the turbulence, shocks, and dynamic activities and of the radio relics and haloes. They have automated X-ray temperature, strain, the brightness of the surface, and density maps by using ClusterPyXT. in its own words, this application does all of the following: it combines, clarifies, and does X-ray imaging in a way that is prepared to handle minimum user interference. Initializing the galaxy cluster for analysis is the first phase of ClusterPyXT. Once you start ClusterPyXT, the user will be asked to enter the cluster information while specifying the Initialize cluster. This takes the name, observation IDs, hydrogen column density, redshift, and chemical abundances of the cluster as reported by recent CIAO with a road map to XMM-Newton[38]. Whilst the consumer can bypass the NH, abundance values to begin, they must be entered before spectral fitting is completed. The next ClusterPyXT stages will start after the necessary data are entered. They have also shown how the developed temperature maps created by this software provide a high-quality image of different phases of the galaxy cluster. ClusterPyXT attribute settings help enhance the analysis behind the science of a galaxy cluster.

In [23] Peterson and his mates study the X-ray spectra of the centers of galaxy clusters and address several potential mechanisms for canceling or distorting the predicted phase of X-ray cluster cooling. They have provided the description of the Cluster of galaxies and Physics behind ICM how X-ray emits from ICM. Then they have discussed the procedures of observing and analyzing these emitted X-ray in detail. After then, they have provided the view of 'X-ray Spectra of Cooling Clusters' along with Early Works regarding Imaging Observations and on Low-Resolution Spectroscopy, Reflection Grating Spectrometer Observations, Recent Spatially-resolved, Spectro-photometric Observations, Observations of Cataclysmic Variables, Definition of the Cooling Flow Problem [23]with proper graph, images to make people understand.

Chapter 3

Target Observation

Some methodologies, with which the data we have processed were extracted, will be provided in detail in this section.

3.1 X-Ray Observation

Usually the temperature inside an ICM is enormously high. This highly temperature gas of ICM causes X-ray emission. X-ray emissions are primarily observed by these three processes named as :

- thermal bremsstrahlung or free-free emission
- recombination or free-bound emission
- two-photon decay metastable level[17].

3.1.1 Thermal Bremsstrahlung

Bremsstrahlung is an electromagnetic emission process that happens when charged particles with substantial energy are slowed down within a very specific range relative to their equilibrium[8]. Even though electrons are substantially more light-weighted than protons, thermal Bremsstrahlung radiation is the most prevalent. Bremsstrahlung generates spectrum continuously with a distinct prole and energy cut-off. Additionally, overlapped lines may emerge, due to the expulsion of K and L shell electrons from atoms during clashes with high-energy electrons.

Since thermal equilibrium in the ICM exists, the single-speed expression of the electron can be averaged over the thermal velocity distribution, and the expression for thermal brake radiation is obtainable. The thermal emissivity of charge Z at a frequency v in a plasma with an electron temperature T_g [8]is defined as,

$$\epsilon_v^{ff} = \frac{2^5 \pi e^6}{3 m_e c^3} (\frac{2\pi}{3 m_e k})^{\frac{1}{2}} Z^2 n_e n_i g_{ff}(Z, T_g, V) T_g^{\frac{-1}{2}} e^{\frac{hv}{kT_g}} \tag{3.1}$$

where ne and ni represent the electron and ion number densities, respectively, the emissivity of a material is defined as the energy amount emitted per unit of time,

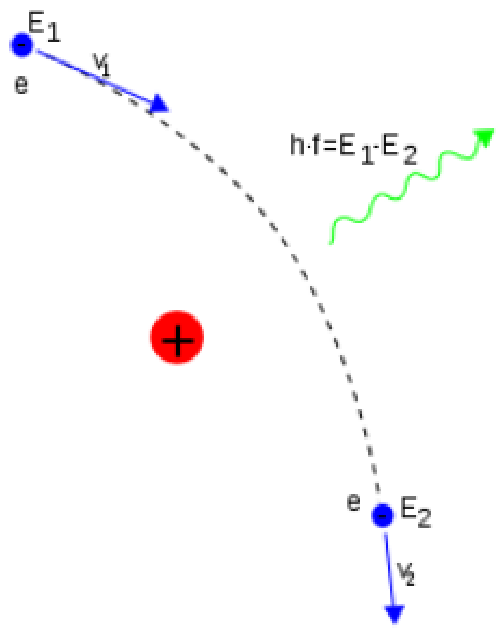

Figure 3.1: Bremsstrahlung radiation is depicted in a simple schematic design. While passing near a proton, an electron (blue) slows down (red). Because it loses some energy (E1E2) via bremsstrahlung radiation, its energy (E1) and velocity (v1) before the interaction are greater than the energy (E1) and velocity (v1) after the encounter[36]

frequency, and volume

$$\epsilon_v \equiv \frac{dL}{dVdv} \tag{3.2}$$

The Gaunt factor $g_{ff}(Z, T_g, v)$ substitutes for quantum mechanical effects and distant collisions[8], and is characterized as a gradually evolving function of frequency and temperature[5]. From the X-ray spectra and the X-ray flux, the atomic number density of the ICM gas may be estimated.
The substantial radiation emissions of the clusters give excellent justification for brake radiation as the major emission mechanism. The strong $7keV$ Fe-line observed in most clusters cannot be explained by any mechanism other than thermal[4]. However, this emission occurs very naturally in the bremsstrahlung model when the metallicity ($\sim 0.3Z\odot$) is near that of the sun[4].

3.1.2 Spatial distributions of the cluster components

All functional forms can describe the ICM gas and dark matter density distributions of a non-interacting cluster in hydrostatic equilibrium. Typically, the X-ray emitting gas portion is located in the cluster's middle. Since the early days of X-ray observations, it has been believed that clusters emit X-rays in a diffuse or prolonged manners. The -model can be used to estimate the density profile of these diffuse X-ray sources[6].

$$\rho_g(r) = \rho_g 0[1 + (\frac{r}{r_c})^2]^{\frac{-3\beta}{2}} \tag{3.3}$$

where $\rho_g 0$ represents the density of the central gas,rc represents the radius of the X-ray nucleus and β represents the asymptotic slope parameter. In the absence of cooling flows, the gas density profiles of clusters are represented by a model with β == 2/3 coefficient [16]. This profile features a flat core with standard dimensions of rc $200kpc$. This description is sufficient for approximately one-third of all clusters[26]. Conversely, the NFW [11] profile enables the simulation of DM haloes (Dark Matter haloes) at more minor scales. On scales ranging from individual galaxies to dense clusters, the density profile of DM haloes is given by,

$$\rho(r) = \rho_s[(\frac{r}{r_s})(1 + \frac{r}{r_s})^2]^{-1} \tag{3.4}$$

where radius scaling, rs, and density scaling, s depend on the haloes. The cusp of the r_1 density of dark matter corresponds to a finite and sharp peak in the middle. This universal density profile is used to estimate the cluster's total density profile (DM+gas). Although the addition of gas can alter this profile, DM dominates in clusters and the total density profile should remain steeper than the central gas profile [29]. After measuring the gas and total density profiles using equations 3 and 4, one can measure the dark matter density profile as follows:

$$\rho_{dm}(r) = \rho(r) - \rho_g(r) \tag{3.5}$$

Clusters that match the centrally peaked profile usually have an undisturbed ICM and are centered on a giant elliptical galaxy that marks the location of the DM peak. Within a radius of approximately 100 pcs of these clusters, the ICM temperature decreases sharply towards the middle, while the gas density and relative abundance of heavy elements in the gas increase [29]. Thus, in the central area, a cool, dense, and metal-rich core is formed [26]. Outside of this field, the radial temperature profile reverses, i.e., temperature decreases again as one approaches the periphery, but entropy increases.

Generally, the ICM gas is resistant to convection[29]. During convection, a bubble grows adiabatically from the central regions, retaining its entropy. If the surrounding material's entropy decreases with radius, the increasing gas parcel will remain lighter than the surrounding medium at constant pressure. Thus, a negative entropy gradient is needed for the onset of entropy, which is not the case in typical galaxy clusters. However, convection in clusters can be triggered by central AGN (Active Galactic Nuclei) activity.

Additionally, microscopic heat and momentum transfer in dilute plasmas, such as those found in galaxy clusters, occur mainly along magnetic field lines. This anisotropic transport can have a significant effect on the plasma's convective stability. In that case, entropy and temperature gradients can no longer be used to assess convective stability [10].

3.2 Cooling flow

The X-ray brightness of the ICM gas [30] in a cluster is calculated using the formula $L_x \propto n_g^2\sqrt{T_g}$,while the energy is calculated using the formula $E \propto n_g k T_g$. Thus,$t_c = \frac{E}{L_x\sqrt{Tn^-1_g}}$ is the cooling time of the gas. The gas density drops as the radius increases. As a result of its higher density, the gas at the center cools faster.

We can define a cooling radius r_{cool} within which the ICM gas and the $t_{cool} \sim t_{thubble}$ can efficiently cool. As the gas cools, the pressure drops, the gas pushes inwards, the density in the center rises, and the core gas cools even quicker. Cooling flow was named after the inward concentration of gas.
Cooling flows were observed to have a

- Centrally peaked surface brightness profile
- Low ionization lines in soft X-ray spectra
- A decreasing temperature gradient towards the center
- Low energy absorption features.

However, no clear proof of the gas's bulk motion was discovered. As per the homogeneous model of cooling flow, the gas at each radius has the same temperature and density and flows inwards under the surrounding gas pressure. It necessitated a constant rate of mass deposition. However, in that case, all of the cluster's gas should be concentrated in the middle, which is not valid. Thus, an inhomogeneous cooling flow model was proposed, requiring gases of varying temperatures and densities to coexist at all radiuses. Different phases of gas are in equilibrium with one another in terms of pressure. As a phase cools below 106 K, it loses pressure equilibrium with the surrounding phases, which begin to flow inward. The vast majority of cooling gas never makes it to the middle. It was uncertain what induced density inhomogeneity in the sense of a cooling flow model. No direct evidence of multiphase ness or bulk motion of gas was discovered later through higher resolution X-ray observations [29]. Furthermore, no cluster with a minimum temperature of less than 1 keV was discovered. However, the cooling flow model estimated that the gas would have a temperature of less than $0 \cdot 1keV$. If the gas does not cool to a temperature of less than $1keV$, it will not be deposited in the middle. As a result, we can find no bulk motion of the gas. Observations with Chandra and XMM-Newton [25] revealed that the central portion of the ICM gas is far from comfortable as it interacts with the central AGN. Indeed, heating the ICM may be necessary to control the cooling flow. Two such heating sources are known: contact with AGN in the cluster's central 20-30 kpc and conduction from the cluster's large heat reservoirs. They may also cooperate in quenching cooling flow, as the mixed models say.

3.3 Cold fronts (CF)

Cold fronts were discovered for the first time in a high-resolution X-ray picture of A2142, a merging cluster. Significant X-ray surface brightness edges were discovered in the cluster's central region [14][8]. Even earlier, a similar edge in A3667 was found, which was perceived as a shock front at the time. When an object or disturbance moves faster than the speed of sound inside the surrounding medium, shock fronts are formed. Thus, gas downstream of a shock wave is denser, cooler, and has a more significant pressure and temperature than gas upstream of the shock wave[7]. Cold fronts are the polar opposite of hot fronts; the denser and brighter gas downstream is hotter[14]. Surprisingly, cold fronts were well-known in meteorology, where the concept is defined similarly to how it is defined in astrophysics [27]. The

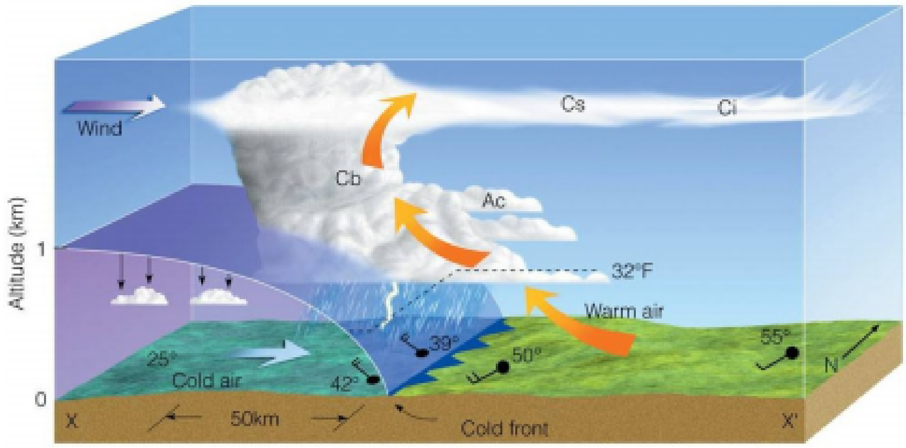

Figure 3.2: shows a cross section of a cold front in the Earth's atmosphere. Adapted from [27]

upstream side's warmer air is raised up and over the downstream side's cold air. The upstream side's warmer air is raised up and over the boundary's cold air. The frontal boundary is very abrupt, which may result in violent thunderstorms and showers. Figure 3.2 represents a visual representation of a cold front forming in the Earth's atmosphere.

Leading up to the release of Chandra, it was not easy to obtain sufficiently accurate temperature profiles around density edges. For the first time, Chandra's observations allowed the visualization and extraction of the jumps' temperature profiles. Cold fronts can be detected by intercepting the brightness edges of an X-ray image with surface brightness and temperature profiles [18]. Assuming the ICM has spherical symmetry near the cold front candidates, these projected profiles allow us to model the underlying gas density and temperature using parametric step-like distributions (see details below). Furthermore, temperature profiles intercept the X-ray image's brightness edges. Assuming the ICM has spherical symmetry near the cold front candidates, these projected profiles allow us to model the underlying gas density and temperature using parametric step-like distributions (see details below).

Pressure increases gradually or changes very little during cold fronts, as an increase in density is compensated for in the ideal gas equation by a decrease in temperature[15]. The X-ray images of A2142 and A3667 are shown in figure 5 as an ideal example. The picture of A2142 indicates two sharp brightness edges, one to the north-west and one to the south of the cluster core. A prominent edge can be seen to the south-east of the center in A3667.

Temperature and X-ray brightness profiles derived from the regions surrounding A2142's cold fronts, along with their best-fit density models and corresponding pressure profiles, are shown in figure 3.4. The regions from which they were extracted are indicated in panel (a) of the figure by red sector annuli. Both edges' brightness profiles lead to the projection of an abrupt, spherical jump in gas density. In panel (d), the best-fit radial density models are shown, and histograms of the density projections at various radii are superimposed on the brightness details. Since the exact three-dimensional geometry of the edge cannot be known, some assumptions must be made when performing this type of fitting[26]. First, the discontinuity surface's curvature along the line of sight is identical to that in the sky plane. Second, that the centers of the radial profiles and three-dimensional models correspond to the front's center of curvature, which is often offset from the cluster center[26].

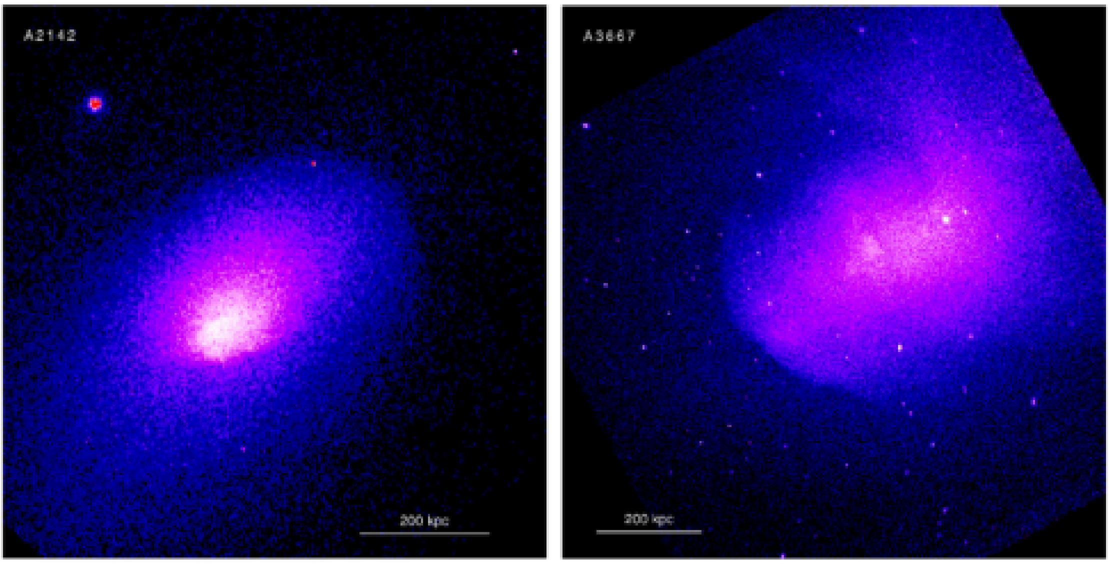

Figure 3.3: Chandra X-ray images of A2142 and A3667 merging clusters. In A2142, two density edges are visible: one to the north-west between black and blue and another to the south of the middle between purple and blue. In A3667, to the south-east of the main, a very prominent edge is evident [26]

The temperature profiles in A2142 demonstrate how cold fronts behave in relation to a shock front. On the basis of thermalized shock energy, the Rankine-Hugoniot jump conditions can be used to characterize the properties of the ICM over a shock front. Consider a component of the shock's surface. At the shock, the tangential part of velocity is constant. Thus, a frame is used in which the shock element is stationary, and the gas does not exhibit tangential motion. Assume that subscripts 1 and 2 denote the pre-shock and post-shock gases, respectively, and that $v_1 = v_x$ denotes the pre-shock gas's transverse velocity[26]. Considering that gas is perfect fluid on either side of the shock jump conditions, the following equations derived from the legislation on mass, dynamism, and energy conservation may be expressed;

$$\frac{P2}{P1} = \frac{2\gamma}{\gamma+1}M^2 - \frac{\gamma-1}{\gamma+1} \tag{3.6}$$

$$\frac{v2}{v1} = \frac{\rho 1}{\rho 2} = \frac{1}{r} = \frac{2}{\gamma+1}\frac{1}{M^2} + \frac{\gamma-1}{\gamma+1} \tag{3.7}$$

Where $r \equiv \frac{\rho 2}{\rho 1}$ is the density jump, is the adiabatic index (in our case 5/3 for mono-atomic gas) and M is the Mach number. After defining temperature jump to be $t \equiv \frac{T2}{T1}$.

we can express the jumps as,

$$t = \frac{\zeta - r^{-}1}{\zeta - r} \tag{3.8}$$

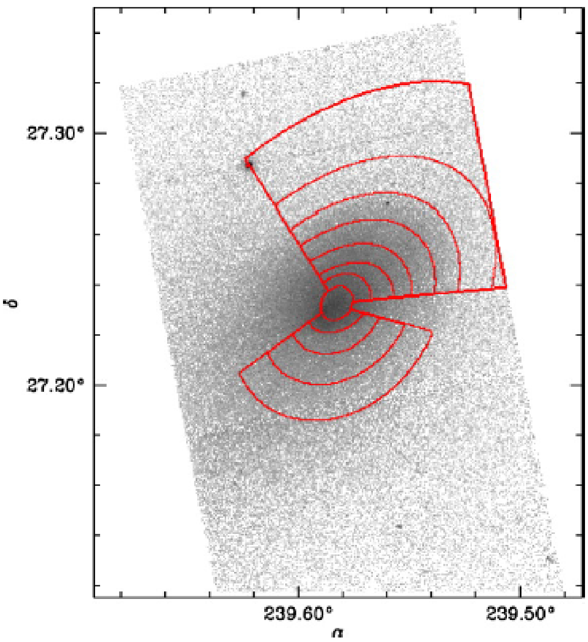

(a) X-ray image of A2142

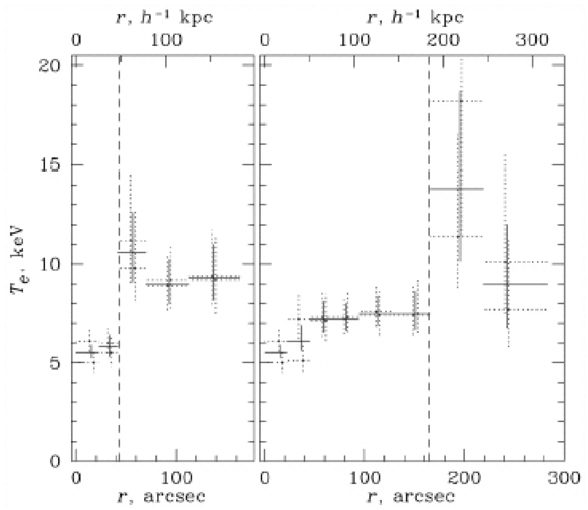

(b) Temperature profiles

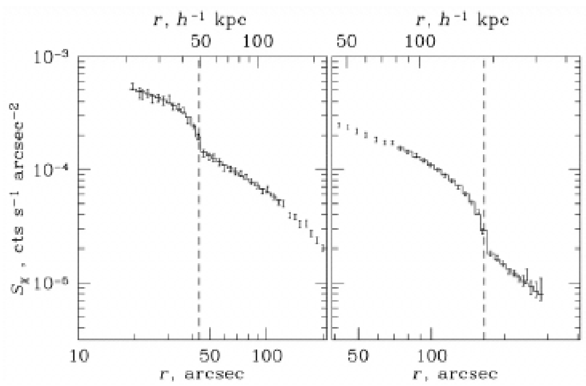

(c) X-ray brightness profiles

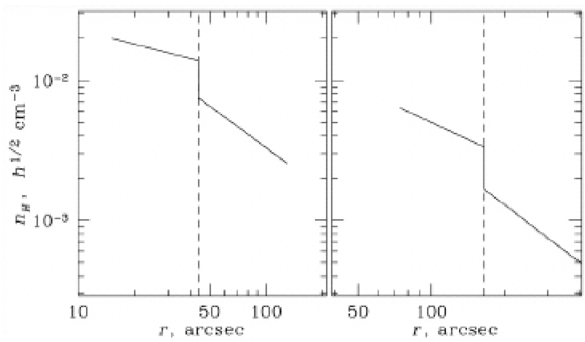

(d) Density profiles

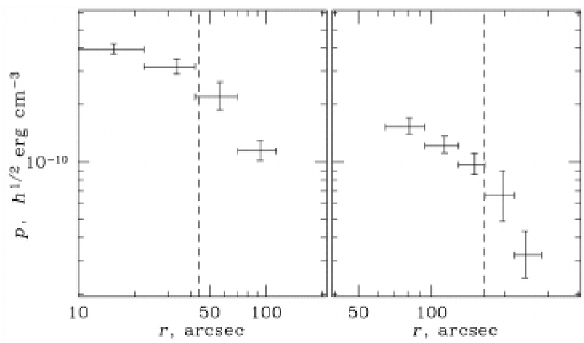

(e) Pressure profiles

Figure 3.4: X-ray image overlayed with separate profiles derived from the two sector annuli. The cluster has two borders, one on the south and one on the north. Beginning with panel (b), the upeer two box corresponds to the southern edge and the bottom three box to the north-western edge of both panels. Histograms reflect the best-fit model in the brightness profile. Vertical dashed lines indicate the locations of density jumps, also known as cold fronts[26]

or

$$r^{-}1 = [\frac{1}{4}\zeta^2(t-1)^2 + t]^{\frac{1}{2}} - \frac{1}{2}\zeta(t-1) \tag{3.9}$$

where $\zeta \equiv \frac{(\gamma+1)}{(\gamma-1)}$

For A2142, the northwestern edge, $r2$ and $T2, 7 \cdot 5$ keV, as observed within the edge. According to the above formulae, if it were a shock, the pre-shock temperature would be $T1, 4$ keV. However, the observed value is substantially different from this and in terms of leap opposite. As shown in the profiles, the outer less dense gas temperature is higher than that of the inner gas, as Chandra's observations determined. This observation is also valid for the southern edge of the A2142 and the southern edge of the A3667.
Since the conventional shock scenario could not describe these edges, alternative explanations for their nature and origin had to be proposed. As previously stated, there is no significant pressure jump across these edges, indicating that the gases on either side of the front are in pressure equilibrium. However, a significant pressure jump is observed at the shock front. On the other hand, the entropy jump can be pretty small in the presence of weak shocks but almost always significant in cold fronts. Because cold fronts are discontinuities in the contact between two gas aggregates with different entropies, one of them could be the cluster's cool core or sloshing gas from the inner radius[15]. This contrast between cold and shock fronts is illustrated in figure 3.7 by the gas density, thermal pressure, and specific entropy profiles across a narrow sector in the famous Bullet cluster, or 1E 0657-56 [26]. There is a cold front at the sector's inner radius, and at the sector's outer radius, there is a shock front. There is a significant density jump at both edges. Pressure is nearly constant along the inner edge but significantly decreases along the outer edge. In comparison to the outer edge, entropy increases very rapidly at the inner edge.
Another example of the cold front's nature came from the observation of A2142's photon image. The left panel of figure 5 clearly shows that the cluster's northwest edge is shaped like a comet as if the surrounding gas is flowing around the inner comet-like gas aggregate. Based on this type of observation, M00 proposed that cold fronts are discontinuities of contact on the borders of gas clouds that move sub or transonically through a hotter and less dense surrounding gas[26][15]. previously used the term 'cold front' in galaxy clusters to describe the discontinuity in A3667. Cold fronts have been detected in at least two-thirds of all known X-ray galaxy clusters.

3.3.1 A simple cold front model

Figure 3.6 represents a section of the gas flow surrounding a cold front in the ICM. The panel depicts the flow of hotter ambient gas surrounding a stationary blunt body (a). The assumption of stationarity for the dense and cool gas is a simplifica-

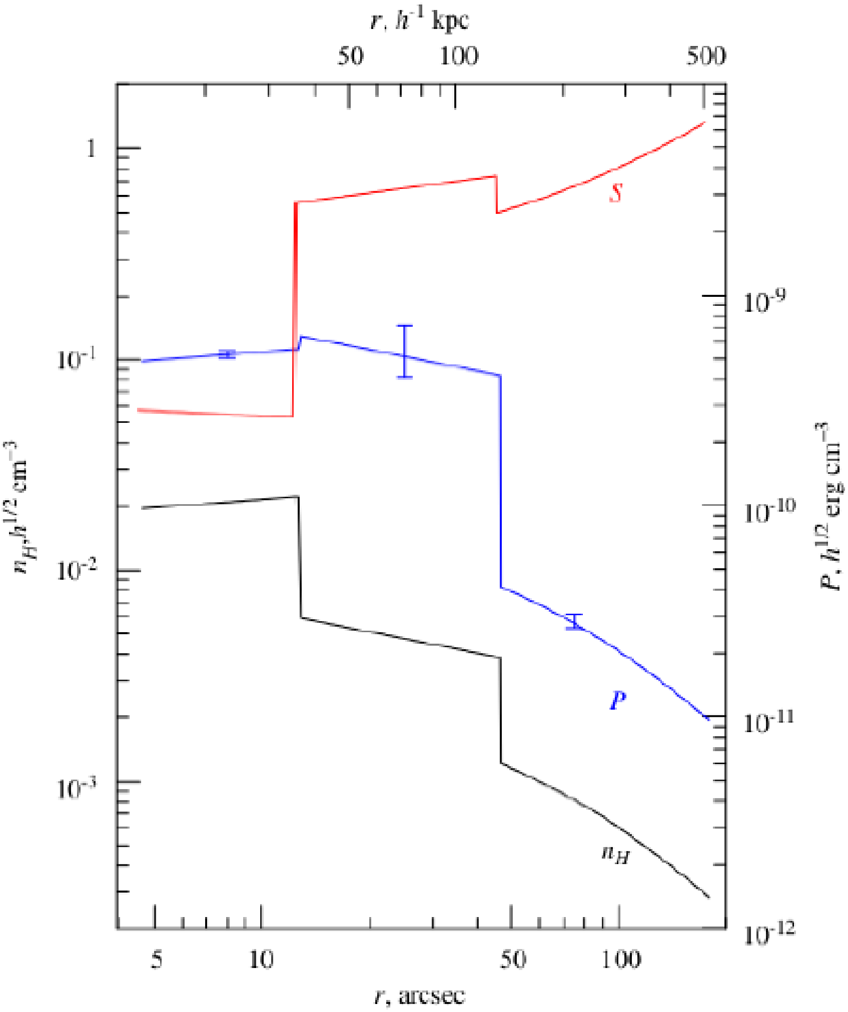

Figure 3.5: Gas (black line), thermal pressure (blue) and specific entropy (rouge) profiles in a narrow 1E 0657-56 section with a shock (outer) front and cold (inner edge)[26]

tion. The flow separates the area into several distinct regions. Near the tip of the gas body (zones0) a stagnation region is formed where the speed component along the symmetry axis becomes zero. External hotter gas slows at the leading edge but accelerates again as it is squeezed to the sides. Thermal pressure increases as one approaches the front and is continuous across the front in the stagnation region. However, because the stagnation region is too small and complex to detect due to line-of-sight projection, one may observe jumps in the pressure profile of a moving cold front[26].
As the gas is adiabatically compressed, the density and temperature of the ambient gas increase near the stagnation region[8]. The outer gas's pressure is assumed to be equal to the pressure in the free stream region (zone 1) [26].In general, thermal pressure from the gas within the cold front is equal to the combined external thermal pressure and ram pressure from the gas. Thus, the difference in thermal pressure across the front directly corresponds to the ram pressure exerted by the flow on the blunt-body. This determines the cloud's speed.The ratio of a stagnant point thermal pressure (p0), which is similar to the cloud pressure (zone 0'), to a free stream thermal pressure (p1), directly affects the cloud rate. Equation 11 gives the formula for this ratio, where M1 is the cloud's Mach number in terms of sound speed in open space. The adiabatic index in the region of streams and ($\mu = 5/3$ for mono-atomic gas). The proportion is plotted as a function of M1 in panel (b) of figure 3.6.

$$\frac{p0}{p1} = (1 + \frac{\gamma - 1}{2} M_1^2)^{\frac{\gamma}{\gamma-1}}, M_1 \leq 1 \tag{3.10}$$

$$\frac{p0}{p1} = (\frac{\gamma + 1}{2})^{\frac{\gamma+}{\gamma-1}} M_1^2 (\gamma - \frac{\gamma - 1}{2M_1^2})^{\frac{-1}{\gamma-1}}, M_1 1 \tag{3.11}$$

For numerous clusters harboring cold fronts, the Mach number of the gas cloud has been established. For example, $M1 = 1 \pm 0 \cdot 2$ was computed for A3667 [14], which corresponds to a cloud velocity of 1400 ± 300 km s^-1. The Mach number in 2A 0335+096 was measured by [35] to be $0 \cdot 75 \pm 0 \cdot 2$.

3.3.2 Cold front classification

A sufficient number of cold fronts have been identified to allow for the development of a classification scheme. At least six distinct types of cold fronts have been discussed in general terms in the review[26]. They still can be broadly classified into two types: fusion of cold fronts and non-fusion of cold fronts.

Merger cold fronts

The cold front is the boundary between two unmixed gas aggregates. These two gases may originate from distinct clusters or the same cluster. The former occurs in major merging clusters undergoing a discernible violent merger, whereas the latter occurs in non-major merging cool core clusters. CFs can appear to be in two phases in major-merging clusters: stripping and slingshot. On the other hand, they appear primarily as a result of gas sloshing in non-major merging clusters.

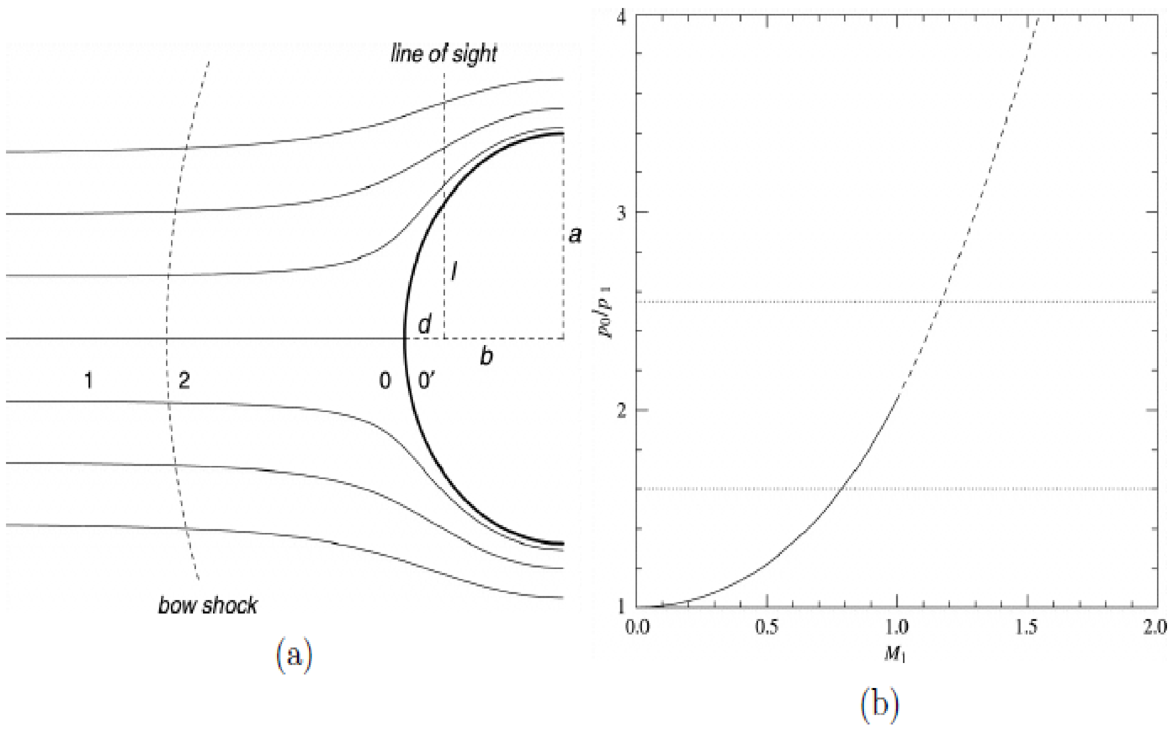

Figure 3.6: (a) Geometric depiction of the surrounding gas flow and past the spheroidal cold front. Zones 0 and 1 indicate areas close to the stagnation point, inside the free flow without interference, and beyond the possible bow shock. Point 0' is included in cold gas. (b) Pressure ratio at stagnation point to free stream pressure depending on free stream Number Mach. The solid and dotted lines signify subsonic and supersonic regimes. According to[26][14]

Stripping CFs:

When two subclusters join, their gas halos' outer regions are shocked and stopped, but the gas in the interior regions is frequently dense enough to resist shock penetration. These surviving gases remain linked to their hosts in dark matter and undergo ram pressure from the ambient hotter gas. Ram pressure drives the remaining gas out of their potentially gravitational wells. The subclusters can be removed entirely depending on the gravitational potential, the density of the environmental gas, and the fusion speed as $Pram = \check{C}ambv2$. If it lives, it will be trapped behind its dark matter peak by gravity. The ambient gas flows around it and creates a cold front. This is the removal of the cold fronts. For example, 1E 0657-56[26]

Slingshot CFs:

Multiple cooling flow clusters are associated with cold fronts but do not appear to have recently merged (strong gas flow, moving sub-cluster remains, etc.). Compared to major-merger CFs, these fronts have a tiny density jump and are primarily found within or on the borders of the cool core, i.e., within a scale of 100–200kpc from the center. They are arc-shaped and frequently center on the gas density peak of the cluster. At times, multiple such CFs can be identified at varying radii from the core. CFs were discovered in over half of the cooling flow clusters, indicating that they are relatively common. Given our limits in recognizing CFs due to projection effects, we can state that the majority, if not all, of the cooling flow clusters, contain one or more CFs. Cold faces are called as a consequence of the sloshing motion of the center cool gas of the cluster in the potentially well[8]. These cold fronts are critical to the validity of our thesis. As a result, a separate section will be devoted to the origins and evolution of these species.

Non-merger cold fronts

Although sloshing CFs are not a direct product of a merger, many, if not all of them, require a prior, minor merger. However, merging is not the sole method for obtaining CFs. There are numerous hypotheses on the formation of CFs via a variety of different mechanisms. In MV07, three such CF kinds are specified.

AGN-induced CFs:

A cooling flow cluster's central gas can be easily disturbed. Sloshing can also be created theoretically by bubbles blasted by the central AGN [34]. Jets from radio-loud AGNs are previously known to inflate bubbles or lobes in the ICM by displacing the X-ray-producing plasma. In an X-ray image, these bubbles look like holes. The possibility of causing sloshing through this bubble has not been thoroughly investigated. However, particular works indicate that it is conceivable. A bubble rising from the inner region owing to buoyant force may push the low-entropy inner gas to the outside regions. When this pushed low-entropy gas collides with higher-entropy gas in the outer areas, CFs can form.

Ripples:

As observed in the Perseus cluster, it has been postulated that sound waves from the center AGN explosion can produce very modest brightness margins. Due to their subtlety, they are heavily influenced by projection, and the temperature jump is likewise insignificant due to the weak shocks [26]. As a result, they are challenging to identify.

Iron front:

The X-ray image of the galaxy group NGC 507 revealed an unusual type of brightness edge [34]. According to its spectral study, the brightness edge is mainly caused by differences in metal abundance [26]. On one side of the boundary, the gas contains a disproportionate amount of heavy elements. As a result, it is referred to as the iron front.

3.3.3 Gas sloshing

As previously stated, CFs may form within a radius of roughly 100 kpc in the cold cores of non-major merging clusters [14] discovered one such cold front in A1795, one of the most laid-back neighboring galaxy clusters. They discovered that the gas that forms the cold front is not in hydrostatic equilibrium within the cluster's gravitational potential. Figure 9 depicts the X-ray surface brightness, temperature, best-fit density, pressure, and mass profiles inside a sector along this cold front.
The presence of a cold front can be inferred from the brightness (a) and temperature (b) profiles. Additionally, it is entirely compatible with a density model. We can observe from the pressure profile that pressure is entirely continuous throughout the cold front, implying that there is essentially no relative motion between the cool dense gas and the ambient medium. Given that the two gas parcels are in pressure equilibrium, one would anticipate them to be in hydrostatic equilibrium within the cluster's gravitational potential. However, the aggregate profile paints a different picture. The mass profile was derived using the temperature and density profiles and the hydrostatic equilibrium assumption from equation 1. The solid lines depict the enclosed mass at various radii within the sector containing the cold front.
In contrast, the dashed lines depict the mass profile in a sector on the other side of the center without a density discontinuity. If the gas parcels in the cluster potential are in hydrostatic equilibrium, the mass profiles from both sectors should be identical[8]. Indeed, the situation is identical outside the cold front. However, the mass profile inside the cold front is significantly different, showing that it is not in hydrostatic equilibrium. However, because it is in pressure equilibrium, we can define it as having zero velocity. As a result, M01 hypothesized that the gas had reached the maximum distance from the center at which the velocity is zero, but the centripetal acceleration is not observed that there was no first discovery of unphysical mass discontinuity in the relaxed RX J1720.1+2638 cluster[15].
M01 presented a gas sloshing mechanism to account for this discontinuity. According to the hypothesis, the gas creating the cold front was displaced from the central dark matter peak by a disturbance and is currently sloshing relative to the potential minimum. Sloshing motion is quite simple to comprehend when viewed through the lens of a glass of liquid. When a disturbance is put into the glass, the liquid

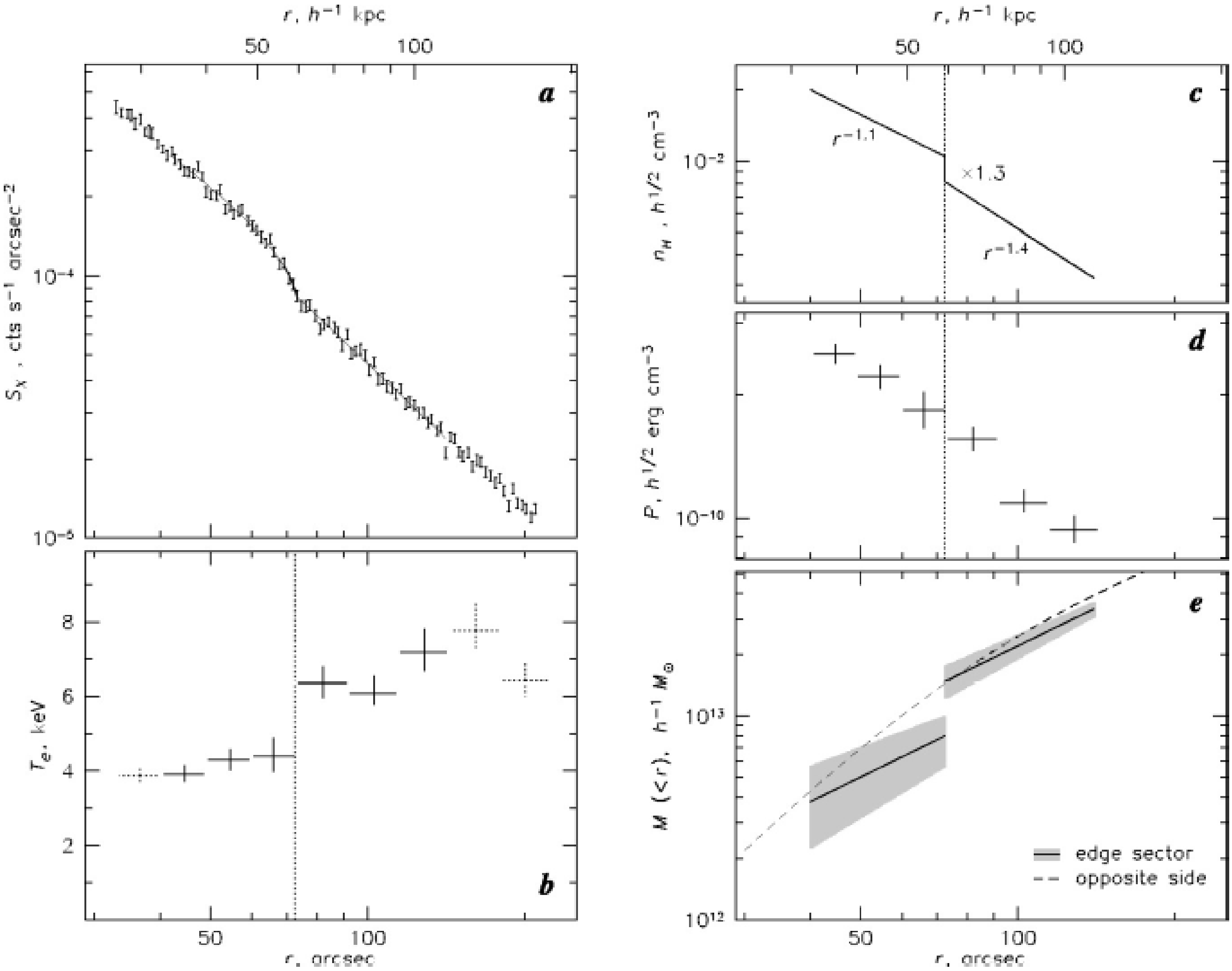

Figure 3.7: All profiles of the cold front sector in A1795 were retrieved. (a) The solid line is the best fit density model presented in the panel (c). (b) Projected profile of gas temperature. (d) Pressure profile and (e) Total contained mass, estimated by hydrostatic balance, in function of the radius. Solid lines represent cold front profiles, while the struck line shows the profile in the opposite sector where no edges have been spotted [14]

sloshes inside. The observation of cool dense gas at its maximum displacement with zero velocity but a non-zero centripetal acceleration is compatible with the sloshing model. Additionally, a cool gas filament stretching from A1795's central cD galaxy toward the cold front has been seen, indicating that much of the center gas is swirling around the cD galaxy.
However, for this scenario to be operated, some disturbance must first counteract the central gas peak. One of the most frequently cited explanations is the collapse of a sub-cluster in the distant past. Bubbles in the ICM caused by a central AGN were also considered as a way to counterbalance the gas peak. However, neither a merger nor core AGN activity was seen in two of the least disrupted clusters, A2029, and A1795 [14]. Thus, in order to have a better understanding of the process, simulations are required.

3.3.4 Simulation of gas sloshing

We see no obvious evidence of a massive merger in the clusters of galaxies with relaxed cooling flows that host cold fronts. However, the beginnings of gas sloshing may have been caused by a tiny merger in the distant past. Thus, an intriguing simulation target may be to determine if a tiny merger might cause disturbance in the central gas peak while leaving no sign of the merger elsewhere provided one such simulation in [20]. Their simulation revealed the following:

- A minor merger can readily set off cool gas in the cluster's center; Cold fronts generated by the sloshing of this offset gas can persist for gigayears.[40]
- The only requirement is that the central cluster has a steep entropy profile, typically the case with cooling flow clusters.
- Even if there is no gas during the fallen subcluster during core crossing, the major disorder that causes the main mass peak (which includes gas and dark matter) to relocate compared to the nearby gas.[20]
- Following the core passage of the in-falling subcluster, this offset peak undergoes a quick shift in the direction of motion. The cool gas peak is pushed from the dark matter peak by the abrupt shift in ram pressure.
- If the impact parameter is more significant than zero, the cool gas develops rotational momentum and sloshes in a spiral pattern.
- If the sub-cluster keeps its gas throughout the merger's initial phase,

The central cluster's cool dense gas is more easily separated from the DM peak. Subsequently, some of the offset gas and possibly some gas from the subcluster fall back toward the DM peak and begin sloshing [20]. However, in this instance, some remnants of the merger will remain.
They might conclude from these data from the simulation slices that cold fronts at the centers of relaxed clusters, which are frequently spiral or concentric arcs in shape, are most likely formed by interactions with small sub-halos stripped of all their gas during the early in-fall stages. In the next sections, certain features of the simulation will be discussed. We will begin with the gasless subcluster in-fall scenario because it is the most straightforward and pertinent to the thesis.

Figure 3.8 illustrates some of the findings from a slice of the simulation of a gasless subcluster colliding with a main cluster five times its mass, using a $500kpc$ impact parameter. The sub-first cluster's core passage occurs $1 \cdot 37Gyr$ after the simulation begins, at a distance of $150kpc$ from the main cluster center [20].

Gas-DM displacement

As illustrated in Figure 3.8, the sub-cluster makes two passes near the center approximately $1 \cdot Gyr$ and $4 \cdot 2Gyr$ after the simulation begins. During the first transit, the gas and DM peaks follow a spiral trajectory relative to the main cluster's center of mass (white cross). The DM and gas are attracted by the same gravitational force and begin to migrate toward the sub-cluster. However, as they travel into the core, the direction of their velocity rapidly changes (compare the arrow directions in the image at $t = 1 \cdot 43and1 \cdot 6Gyrs$). For the gas peak, this translates into a shift in the direction of the ram pressure. As seen, the direction of ram pressure is upward at $2 = 1 \cdot 6Gyr$, in contrast to the prior downward direction. Due to this modification, the gas peaks shoot up from the cluster's potential minimum like that detailed in Section (cold front classification). Indeed, another small shock produced by the sub-cluster in-fall acts in conjunction with ramp pressure to initiate the gas peak as indicated in AM06. The following section states that the first cold front emerges when the offset gas begins to descend back toward the DM peak. It should be noted from the graphic that the first CF appears at $t = 1 \cdot 7Gyr$.

Onset of gas sloshing

When the subcluster separates from the central cluster, and the displacing force weakens, the displaced gas peak begins to revert to the potential minimum. The details of this motion are depicted in figure 3.9, which shows a zoomed-in view of the true for clusters such as A2029. The first panel of the graphic depicts the temperature map $1 \cdot 6$ Gyr after the simulation started, i.e., when the gas peak was initially displaced from the DM peak[26].

As some of the displaced cool gas is moved further away by ambient gas flow, it expands adiabatically. However, the coolest part of the gas reverses direction and begins sinking toward the potential minimum, similar to the commencement of RayleighTaylor instability (RTI). The onset of RTI can be visualized as two layers of immiscible fluid, one heavier than the other and subject to gravity. The equilibrium is unstable in this case in the presence of perturbations or disturbances [14]. As the heavier material travels below the effective gravitational field and the lighter material is moved upward, an unstable disturbance will grow and result in the release of potential energy. This occurs twice in the simulation, first at $t = 1 \cdot 6Gyr$ and then at $t = 1 \cdot 8Gyr$ from the other direction [35]. At $1 \cdot 7Gyr$, the downhill traveling cold gas is subjected to the ram pressure of gas flowing upward from the opposing side. Thus, the cool dense gas is retarded and expands sideways into areas of lower pressure, forming a mushroom-like structure. It happens when a gas jet flows via a less dense gas, since Bernoulli's principle stipulates that an increment in a fluid's speed is accompanied by a decrease in pressure or potential energy [41] . Cold fronts are sharp contact discontinuities along the front margins of these mushroom heads.

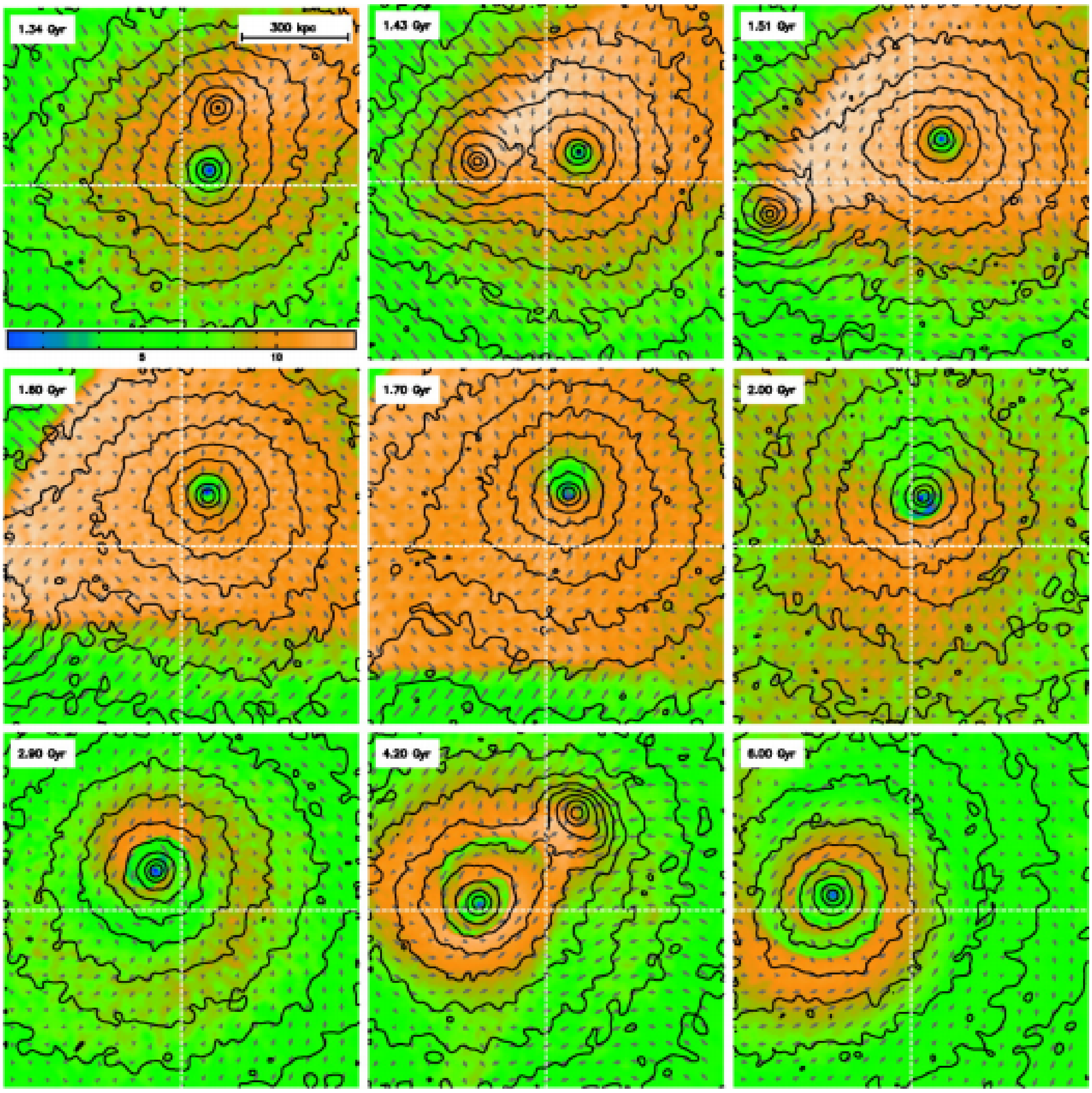

Figure 3.8: Cold fronts evolution generated by the gasless sub-cluster in autumn.The main cluster is five times as big than the subcluster, with a 500 kpc impact parameter. This color map depicts the gas temperature in an orbital plane slice of the simulation. A temperature scale in keV is given underneath the first panel. The arrows indicate the direction of the gas velocity field in relation to the dark matter[9] . The contours (drawn with a spacing of 2) represent the density of dark matter in the nearby area. The intersection of the white dashed lines indicates the center of mass of the main cluster's DM particles[26] According to[20]

Emergence of multiple cold fronts

At $1 \cdot 8Gyr$, we notice that the mushroom head's densest, lowest entropy gas once again separates from the rest and begins descending toward the DM peak [26][19]. A structure at the core of the Ophiuchus cluster resembles this scenario slightly. Meanwhile, the remainder of the mushroom head's gas continues to grow adiabatically outward towards the ICM's areas of lower pressure. At $1 \cdot 9Gyr$, this upward traveling gas collides with downward flowing hotter gas on the opposite side and spreads into a mushroom-like structure, as it did previously. The mushroom stem represents the forward flow of the cold gas, while the head represents the region where the ambient gas's ram pressure impedes it.

This process repeats itself, and when the lowest entropy gasses are reversed in terms of external, higher entropy gas, a discontinuity of contact is generated along with the heads of the mushroom which leads to several cold fronts in the center of the same cluster. As illustrated in the pictures, the mushroom heads are constructed on linear scales that decrease in size. Sloshing of the dense cool gas closer to the center has a shorter period and amplitude than that of the gas at higher radii initially[40] .This time difference brings together distinct gas phases that had initially differing off-center distances and entropies. One must recall that the DM peak oscillates similarly about the center of the mass due to the flyback of the subcluster but over a very long time. The period of the DM oscillation is $1Gyr$, compared to $0 \cdot 1Gyr$ for the sloshing gas. As a result, the DM distribution in the core remains symmetrical in the center, whereas the cool gas sloshes back and forth. DM oscillation, on the other hand, can provide some kinetic energy to the sloshing gas. We now understand how many cold fronts are formed through sloshing motions.However, the particular physical mechanism has not been called into doubt. The pertinent topic here is how an originally continuous gas distribution transitions to a sharp contact discontinuity. In the event of cold fronts merging, it is understandable that the tangential gas flux around an incipient dense gas subcluster may take away the outer layers of the subgas clusters until it reaches a radius where the pressure within the cold gas is equivalent to the pressure outside[26](see figure 3.6) . There is no peeling of the splashing cold fronts. To address the question, we must concentrate on figure 3.10. The three panels depict the simulation at three distinct points in time. $1 \cdot 55Gyr$ is the approximate time at which the cool dense gas of the main cluster reverses direction and begins to descend back towards the DM peak, where it experiences ram pressure from the ambient gas. Each cubic centimeter of gas in the core near the axis of symmetry experiences the same ram pressure during subsonic vibrations[26]. As a result, denser gas suffers less acceleration. In the dense gas, a speed gradient is formed in the direction of the force (in the figure, that would be the downward direction). The outside section of the cold gas parcel with a lower density is then squeezed to the sides, as illustrated in the right panel of figure $3 \cdot 10$. Thus, the inner denser gas gradually escapes and eventually makes contact with the surrounding medium. Based on the simulation findings, AM06 determined that when a smooth gas density peak collides with an ambient gas flow, a contact discontinuity occurs quickly by "squeezing out" the gas layers next to the future stagnation point, which is not in pressure equilibrium with the flow [26]. Such gas is stripped away from the cold front's symmetry axis by the shear flow.

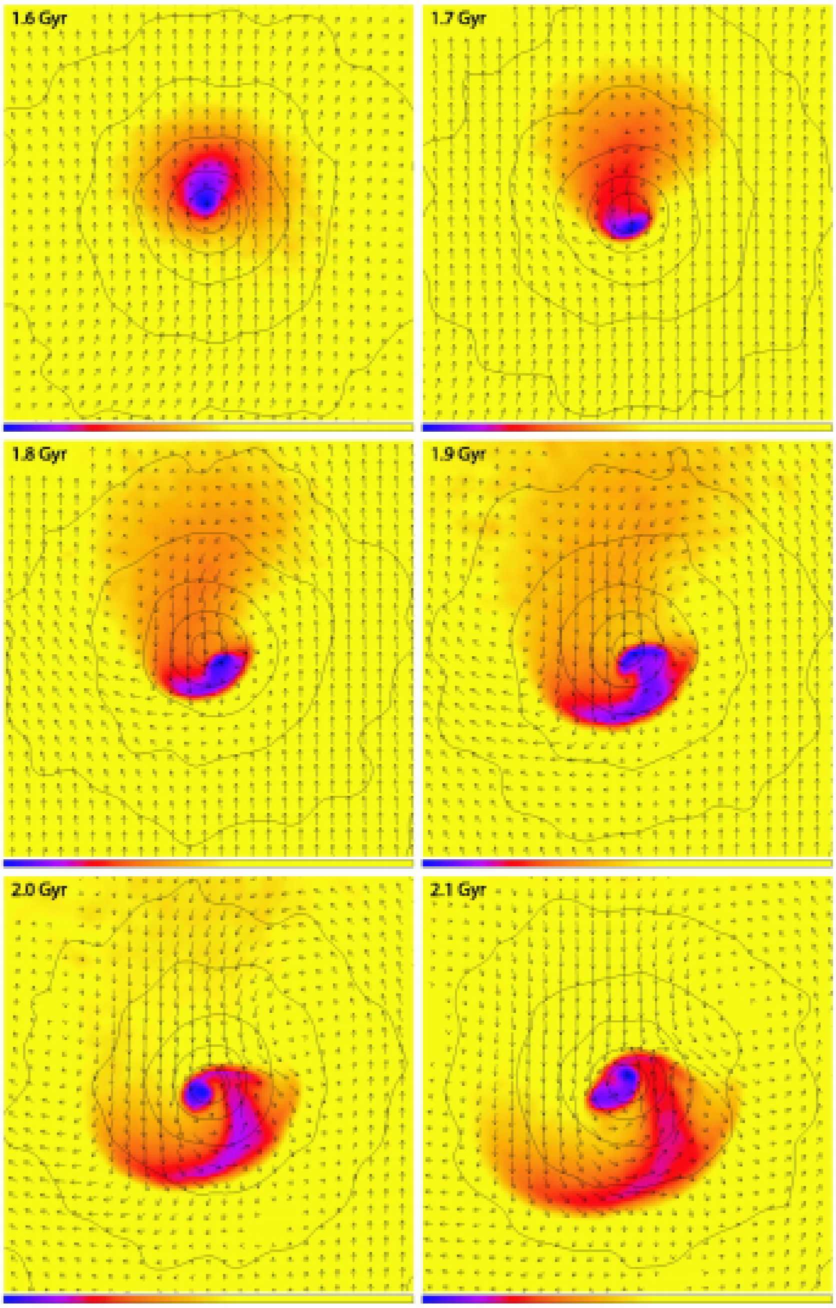

Figure 3.9: Zoomed-in view of the simulated cluster's temperature slices. Blue has a wavelength of 1 keV, while yellow has a wavelength of $7-9$ keV. The contours denote the field of dark matter density. The length and direction of the arrows indicate the magnitude and direction of the ICM gas velocity, with the longest arrow representing $v = 500$ km s1. The panel measures $0 \cdot 25$ Mpc in size. The velocities are subsonic; for example, when $T = 79$ keV, the sound speed is $1300 - 1500$ km s1. According to [20]

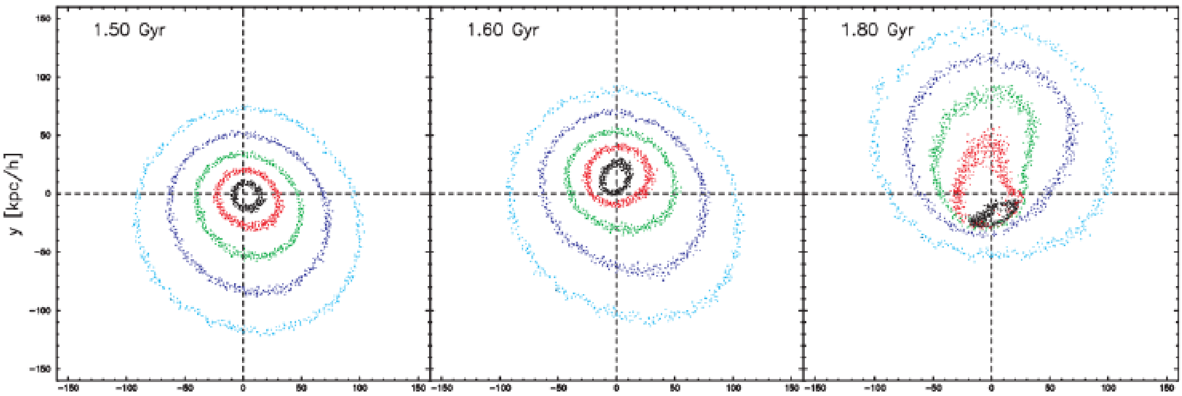

Figure 3.10: illustrates the evolution of simulated particles on the merger plane during the infall of a gasless subcluster. On the right panel, we notice the emergence of a strong contact discontinuity. According to[40]

Spiral structure

In figure 3·8, we can see a distinct spiral pattern generated by the center cold fronts. This picture fits the data of A2029 [42] and the Perseus Cluster[23]. The simulation of AM06 indicated that a non-zero impact parameter defined by the perpendicular distance between the path of the incoming sub-cluster and the center of mass of the central cluster is the only criterion for this spiral configuration. Due to this distant flyby, the central cluster's cool center gas gets some angular momentum and is unable to collapse radially back to the potential minimum. That is why cold fronts do not have a concentric structure but rather a spiral structure.
There is no coordinated spiraling motion at first because each edge is autonomous. Nevertheless, with time, circular motions against the average angular momentum decrease, and mushrooms are asymmetrical. It appears like a gigantic spiraling flow of chilly gas on a massive scale. Low entropy gas flows from the head of a mushroom through the mushroom stalks into the smaller cap.

Chapter 4

Software Overview

Chandra Interactive Analysis of Observations, shortly known as CIAO was first released in 1999 after the launch of Chandra X-ray Observatory in space[22].Chandra X-ray Observatory (CXO) is made for detecting X-ray emission from hot regions of space such as galaxy clusters, explosion of stars, blackholes etc. Though CIAO was originally written for the CXO but later it was released as a general-purpose scientific data analysis system for X-ray astronomy. It has also been used for non-X Ray data.

4.1 CIAO

There are 195 tools currently available in CIAO (version 4.13). These tools are divided into six categories:

- Data Manipulation:Used for binning, smoothing, image calculation, histogram extraction, data statistics,
- Data Preparation:To process or recalibrate data produced by the calibration or unique processing requirements of Chandra pipeline instruments [22].
- Imaging:For imaging data analysis like source detection, creating exposure maps, normalized images, 2D PSF models, calculating image statistics, merging data from multiple observations etc.
- Imaging Spectroscopy:Extract source and background spectra from imaging observations.
- Grating Spectroscopy: To identify and extract spectrums of the origin and the background of Chandra grating findings[22].
- Timing Analysis tools: Light curves are extracted and time fixes are performed.

- Response Tools:Computing effective areas, exposure maps, energy redistribution, software mask etc.

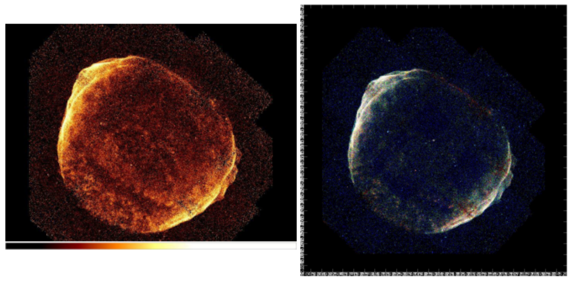

Figure 4.1: Composite mosaic image of supernova remnant SN1006 from 11 separate Chandra ACIS observations using several CIAO tools[22]. Red and blue color indicating no-thermal and thermal emission respectively.

There are also some applications that come with CIAO. Two most prominent applications of CIAO are Sherpa and ChIPS. Sherpa constructs complicated models from basic specifications and fits them to data using statistics and optimization approaches [13]. ChIPS is used for creating interactive plots in a flexible way and adding other features in plots. Data also can be virtualized by the DS9 application.

The CIAO software currently offers Python as the user scripting environment. Experienced users may create their own complicated processes according to the scripting functionality[22]. The easiest way to use Python packages in the latest release of CIAO (version 4.13) is to install CIAO via the conda package manager. (https://cxc.cfa.harvard.edu/ciao/scripting/)

4.2 ClusterPyXT

The central part of our data pre-processing for generating the brightness, temperature, and density map of A3444 is produced with the help of ClusterPyXT along with CIAO. The most recent generation of X-ray telescopes has produced vast amounts of data. The Chandra Database clusters are dispersed across more than a hundred kiloseconds amongst 10 or more different targeted X-ray observations[38]. Although current data analysis techniques enable thorough manipulations automatically, these techniques change seamlessly and simultaneously allows for a significant decrease in wasteful interventions by the users. Spectral fitting is an existing idea but implicating this via user-friendly, open-source, and free-to-access software is marvellously innovative. ClusterPyXT is a pipeline program for automating the development of x-ray temperature maps, pressure maps, maps for superficial luminosity and density maps. It is open and is being actively developed.

4.2.1 Program flow

The observations will be merged and the data products combined; ClusterPyXT mainly automates these kinds of stuff. Every cluster has some common essential entity such as name, metallicity, redshift, the galactic hydrogen column density (NH), Chandra observation IDs, etc. The software downloads the data and merges the findings with their underlying histories when a user wants to identify those entities. The pipeline then eliminates areas from the point source supplied by the user, consisting of high energy events. Following that, the pypeline eliminates user-supplied point source areas before processing high-energy activities.The efficient exposure times are based on the filtering and a map is built that successfully measures the adjustable bin size for every pixel[38]. With the compilation of the spectral fitting, ClusterPyXT provides a temperature map as the final result.

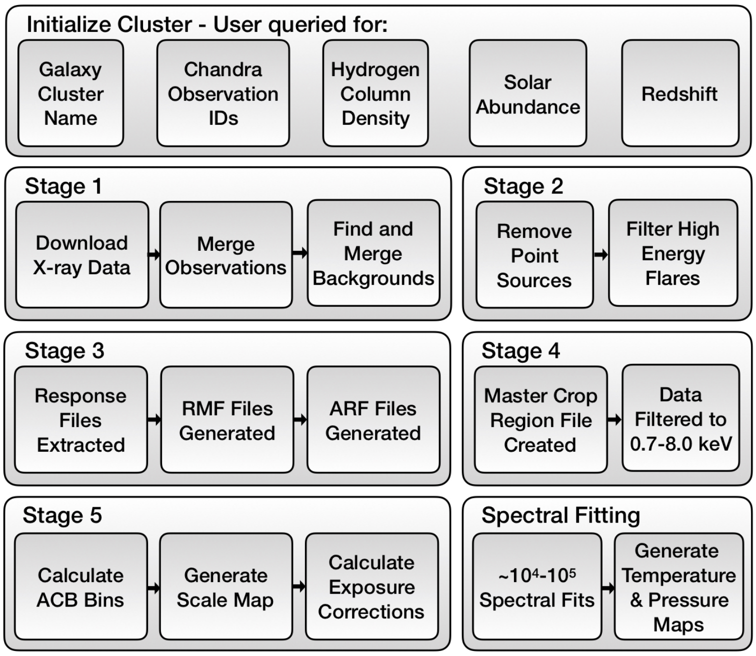

Figure 4.2: The program flow is presented in a block diagram. Cluster initialization, data collecting, data processing, and data product development make up the entire procedure.

4.2.2 Software Processing

The very first stage of ClusterPyXT begins by initializing the galaxy cluster. The user is asked to enter the cluster's information such as 'name', 'the observation IDs', 'hydrogen column density', 'redshift', and 'chemical abundance' relative to solar for the cluster[38] after beginning ClusterPyXT and choosing Enable Cluster. The following levels of ClusterPyXT will begin as soon as the appropriate data has been entered. The primary data collection and processing step is the very first step of the pipeline once a cluster has been synchronized. *"download chandra obsid"* function takes Chandra observation IDs (OBSIDs) as an input downloads all the files related to each observation [38]. Along with these OBSIDs data, this feature downloads all of the files corresponding with every distinct finding. ClusterPyXT's new version only uses ACIS-I CCDs, with ACIS-S operation following in the next big iteration. The data is encrypted when it has been downloaded within each observation. The Chandra-repro mechanism is then used to repurpose each interpretation. This feature creates the bad pixel, level 2 case, and level 2 pulse height amplitude (PHA)

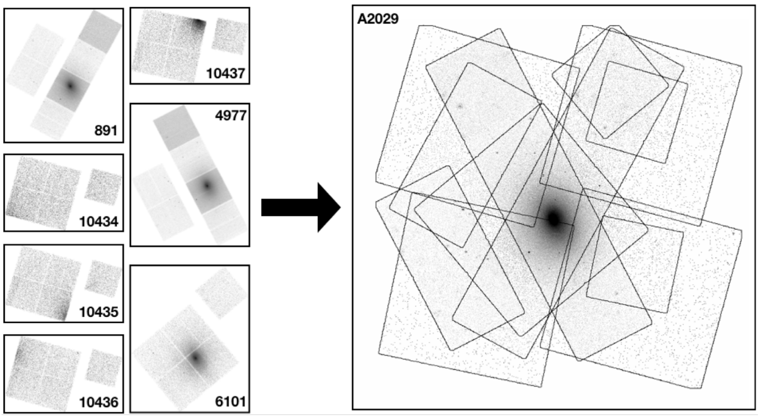

Figure 4.3: Stage 1 of the pipeline downloads cluster observations and backgrounds, then merges them, as seen in A2029. Note that the code's present implementation only uses ACIS-I observations. The next major version will include the integration of ACIS-S observations.

files that are used in the pipeline's later stages. Following reprocessing, a level 2 event file with the CCD ID defined is created for each ACIS-I CCD used in each observation using the dm-copy command. The background files developed in the previous step will be merged with these files to create a consolidated X-ray surface brightness map of the cluster. To adequately attain a temperature match, the history files for every ACIS-I CCD employed in every experiment are deemed necessary. The axis-background lookup function is used to retrieve these files, and the reproject events function is used to reproject the relevant histories, which requires the context approach and good time intervals (GTI) for each phenomenon. The prefix pcad appears in the aspect solution files, which define the telescope's inclination concerning time. The GTIs, or tables of start and stop times for the events, are examined in each of the different ACIS-I CCD level 2 event files prepared in the prior step. The dm-merge command is then used to combine the context files. The pypeline completes stepping one by combining the findings into a consolidated case file and generating intensity balanced images upon history merger. The merge-obs and flux image protocols are used to execute certain phases.The user is then given instructions regarding the operation of the pypeline.

The pipeline's fourth stage is comparatively brief to other stages.The user must first create an area file that has a box that contains all of the picture segments that should be analyzed [38]. This area is clipped out of the final shot. The findings and histories are then filtered to a range of $0 \cdot 7$–$8 \cdot 0$keV.The $0 \cdot 7$–$8 \cdot 0$keV range was chosen since Chandra Proposer's Observatory Guide12 states that it offers the best quantum effectiveness and overall field, resulting in the best high impedance. Following that, the images are merged to be used in the next step.

The last phase in the pipeline, before the spectral temperature matches, is one of the most CPU bound steps. The bins are calculated at this point of the pipeline using an adaptive binning algorithm [28]. The development of the scale map is the first step. The scale map is an image in which each pixel's value corresponds to the radius's value. This radius specifies how far out a circular area must be for a pixel to achieve the user-specified signal to noise ratio. A greater radius is formed at each pixel before the desired signal to noise ratio is obtained. Since the edges

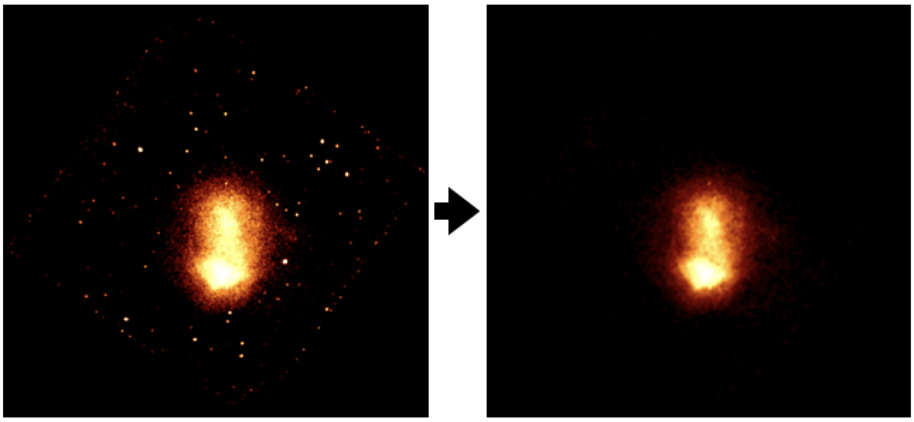

Figure 4.4: Both photos show the X-ray surface brightness of the Toothbrush cluster. The point sources are included in the left image before being excluded by the pipeline. The right image is the source-removed picture that will be used in the pipeline's final stages.

of observations rarely generate sufficient data to provide a reasonable mathematical fit, the image's perimeter will almost certainly be edited out. This state's next move is to create an area file for distinct interpretation, which contains circular territories for each non-zero pixel in the scale diagram.

4.2.3 Spectral fitting

The size of the pixel in the scale map determines the radius of these regions. The successful inspection times for every region is determined once all regions have been established. To appropriately balance each observation, such periods are expected [38]. The last step in this stage is to write the script files that will be used to activate the fitting algorithm. The ending of these document files can be run in a variety of ways. The default fitting protocol addresses all variables except normalization and temperature in an effort to expand the error bars in the resulting temperature plot. The fitting technique deletes pulse invariant (PI) files from event files and replaces them with auxiliary response files and replicates matrix files for each ACB area. The spectral fitting technique is done with Sherpa [28]. The X-Spec PHABS platform was combined with the X-Spec APEC platform. The abundance, z, and NH parameters are all configured to the user input, resulting in a combined model. After that, the temperature (in kT) and standardization parameters are fitted. Although the chosen parameters to fix or fit are hard-coded, any of the aforementioned parameters can be fixed or fitted with a quick update to the code. These fits, along with the related figures and area numbers, are written to a file. The image map also with values of the fitted temperatures is then re projected from the file containing the positive spectral fits. Tiny, medium and high resolutions are available for the spectral fitting procedure. The resolution setting determines how many pixels have accomplished spectral fits [38]. For high resolution every distinct pixel is considered for this fittings process. For medium resolution it uses 3 *3 pixels using the center pixel. Low resolution uses 5*5 pixels in a similar manner. This effectively renders the pixels 3x3 fitting them together using the middle pixel. This is expanded to 5x5 at low resolution. The resultant picture typically shows some binning errors, especially at high resolution. Fig.4.5 shows a depiction of the three resolutions.

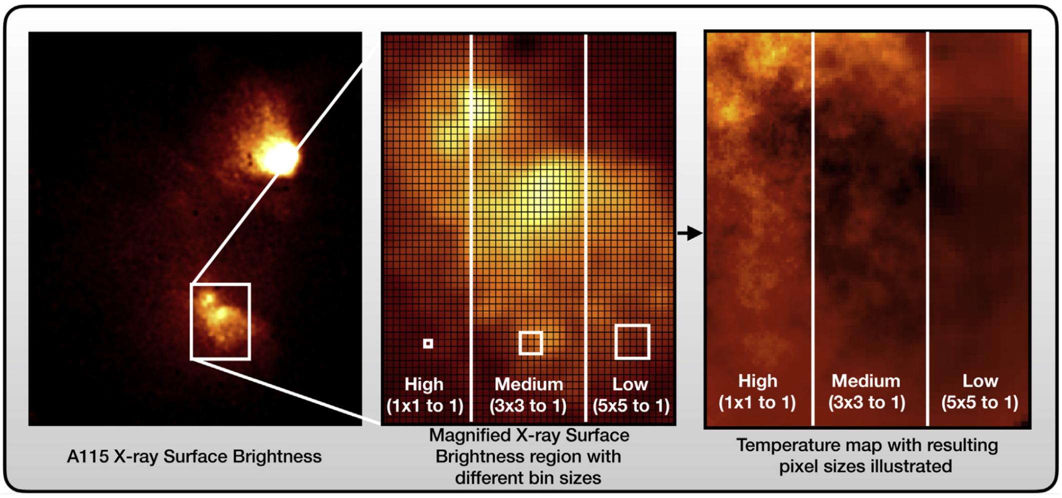

Figure 4.5: The final temperature map shows different resolution levels. The left picture is an X-ray surface map obtained during the early stages of the process. The center panel shows a zoomed-in part of the Southern Subcluster to see the available three-bin sizes. The resolution results for each bin size are shown on the right image: If no resolution is provided, medium resolution is the default (middle). High resolution (left stripe) results in a spectral fit for each pixel in the radiation picture; low resolution (right) leads to the fitting of practically every 5th pixel in every 5th row; The default is medium resolution (middle resolution) if no resolution is provided)[38]

Chapter 5

Workflow

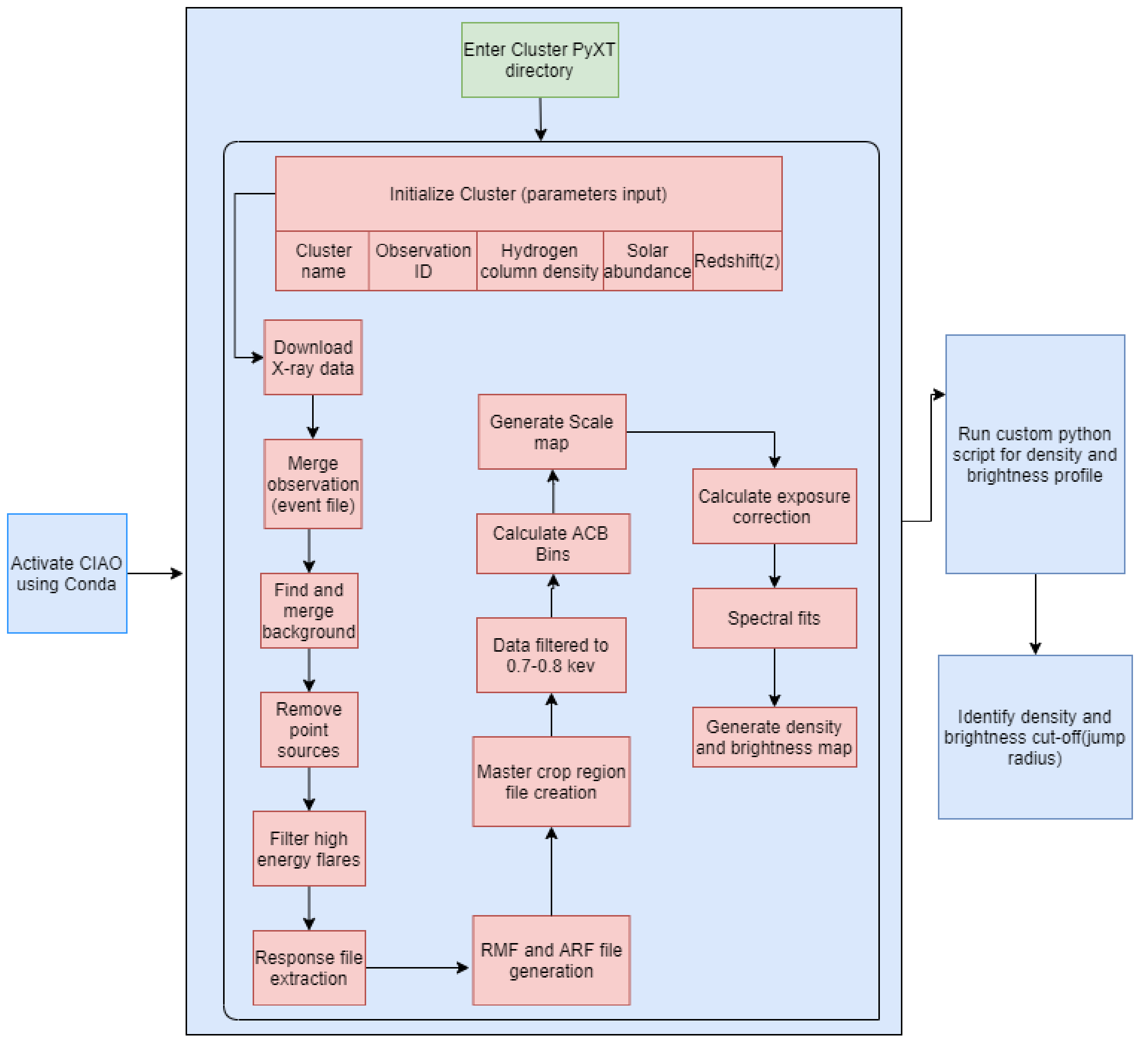

Figure 5.1: Diagram of proposed workflow for mini-halo detection from X-ray data.

5.1 Environment setup

The CIAO (version $4 \cdot 13$) was tested in Ubuntu $18 \cdot 04 \cdot 5$ LTS (Bionic Beaver). So,we set up everything in the Ubuntu $18 \cdot 04 \cdot 5$ operating systems. It is also tested

on Apple macOS $10 \cdot 13$ (High Sierra) through macOS $10 \cdot 13$ (Catalina)[13].
To use python (version $3 \cdot 7$) in the CIAO environment and ClusterPyXT pipeline to work we installed conda package manager. CIAO $4 \cdot 13$ only supports Python $3 \cdot 7$. So, we need to select python $3 \cdot 7$ during conda installation. For using conda we installed the following applications along ciao: For using conda we installed the following applications along ciao:

- Sherpa
- Ds9
- ciao-contrib
- caldb
- marx

For virtualizing and processing output maps using python we installed the following libraries inside CIAO environment using conda:

- Astropy
- Jupyter
- Ipykernel

Now we are all set to go for data downloading and processing.

5.2 Data source and download

First of all, we need to retrieve our X-ray data for our analysis. For this purpose, we used Chandra Data Archive to get necessary data. Secondly, we need to know the observation ID of our galaxy cluster. The Chandra Observation ID of galaxy cluster RXC J1504.1-0248[32] is 5793. At this point, more information is needed to start processing the Hydrogen Column Density, Redshift(z), abundance, and Signal to Noise Ratio. These parameters are discussed briefly below.

5.2.1 Hydrogen Column Density:

In the Galaxy, hydrogen is the most commonly seen element of the interstellar medium. The analysis of hydrogen emissions in its atomic neutral form continuously provides an overview of the different temperature and density regimes of the interstellar medium, the cinematic and morphological characteristics of the galaxy cluster[41].The value of hydrogen column density symbolizes the number of neutral hydrogen atoms (HI) per square cm (cm2) between the observer and the area of observation. For RXC J1504.1-0248 it is $5 \cdot 7E + 20$ (rounded value) on average. We got this value from the web version of the nH FTOOL developed by Lorella Angelini at the HEASARC (High Energy Astrophysics Science Archive Research Center).

5.2.2 Redshift(z)

Because of acting like a wave, light emitted from bright objects produces a Doppler-like shift when the source moves away from us. We know that since 1929, when Edwin Hubble found that the Universe is expanding, most other galaxies are moving away from us[2]. The light from these galaxies has been red-shifted, or relocated to longer and consequently redder wavelengths. The redshift equation is

$$z = \frac{v}{c} = \frac{\Delta\lambda}{\lambda_0} = \frac{\lambda_v - \lambda_0}{\lambda_0} \tag{5.1}$$

Here, λ_v is the perceived wavelength and is affected by radial movement between the target and the observer, and λ_0 is the rest wavelength of the radiation. To express the measured wavelength minus the rest wavelength, the term $\Delta\lambda$ is frequently used. Optical light wavelengths are commonly expressed in Angstroms $(1 = 10 - 10m)$ or nanometers $(1nm = 10-9m)$.[28] When Hubble plotted the redshift against the distance between galaxies, he discovered an unexpected relationship, "the more distant galaxies are traveling far from us quicker". Hubble said, "the faster and smaller a galaxy is, the further it is from us and the faster it is apart, or the recessional speed of a galaxy is related to the space between us."[28]

$v = H_0 d,$

In the galaxy's velocity (in km/sec), d is the galaxy distance (in megaparsecs; $1Mpc = 1millionparsecs$), and the Ho constant is the 'constant Hubble.'We collected the redshift value for RXC J1504.1-0248[8], which is $0 \cdot 2153$.

5.2.3 Abundance:

Metallicity in astronomy refers to the presence of heavier particles than hydrogen and helium in an object. Either hydrogen or helium is the most common physical stuff in the universe, and astronomers are using the term 'metals' in the short term 'all elements with the exception of hydrogen and helium'[37]. For our application, the developer of the ClusterPyXT pipeline suggested using $0 \cdot 3$ as the abundance value.

5.2.4 Signal to noise:

A signal-to-noise threshold is needed for source detection. We used 5 as our signal to-noise ratio value. After entering all the parameter values the CIAO downloads all the data of RXC J1504.1-0248.[31]

5.3 Map generation

Currently, the ClusterPyXT only supports ACIS-I CCDs. Therefore, we are going to use only ACIS-I CCD data for our X-ray observation.
After initializing the parameters and downloading data files, the pipeline merges cluster observations and backgrounds discussed in Chapter 4 . Then, we manually select the sources that are not part of the cluster. The exposure-corrected image

shown in figure 5.2 is created from an ACIS observation of cluster RXC J1504.1-0248 using all the event files. The output image also contains all ACIS CCDs that were under the observation. In our case, we have 4 CCDs for our observation. It is basically a merged surface brightness map.

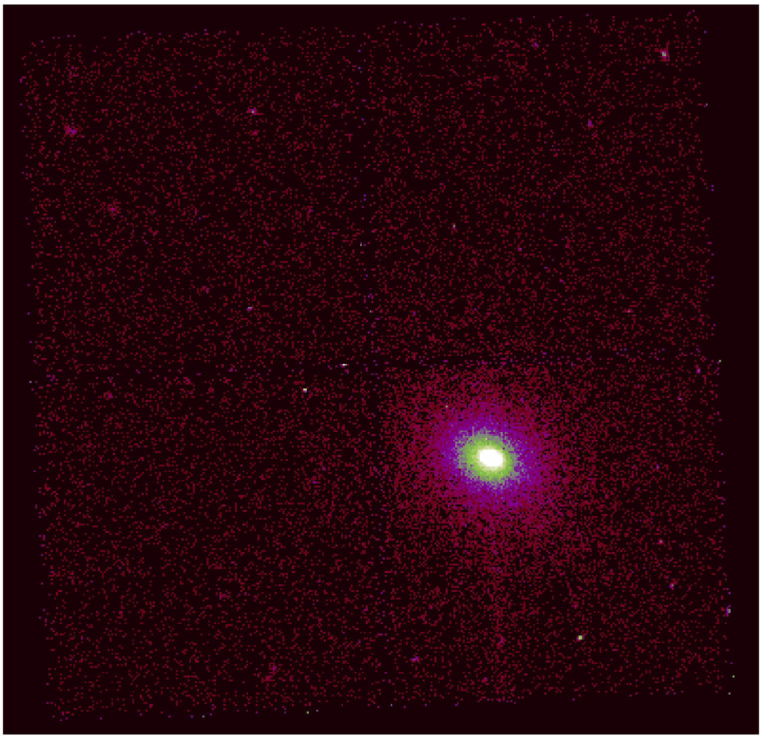

Figure 5.2: Exposure-corrected merged surface brightness map of RXC J1504.1-0248 from event file.

First, we need to remove point sources from the merged surface brightness map from different observations. The observation may have various unwanted objects because of some events like solar flare and other objects on the path. As shown in Fig 20, we identified the possible point sources and possible high-energy flares by observing the area far away from the center of the galaxy cluster. So, we created a region around these point sources to exclude from our analysis and save them as a region file to open later on, in order to process.

Secondly, we need to select our area of interest which we will analyze, so that it can be excluded from the 'deflaring' process. We selected the brightest point of the galaxy cluster and created a region around it shown in figure $5 \cdot 4$. We may need to change this radius if we are unable to see our desired result in future. This region file is saved separately. We choose a radius of 40 from the center shown with a green circle in figure $5 \cdot 4$.

After 'deflaring' we need to extract the RMF and ARF files. ARF stands for auxiliary response file[12] and RMF[12] stands for Redistribution Matrix File. As we can see from figure 5.5 that there are four ACIS-I CCD's in our observation. We only need to consider the CCD, which contains the galaxy cluster and its neighbor. We draw a region circle with a piece of each CCD shown in Fig 5.5. The recombination matrix files map energy-space to detector-recorded pulse height amplitude space.

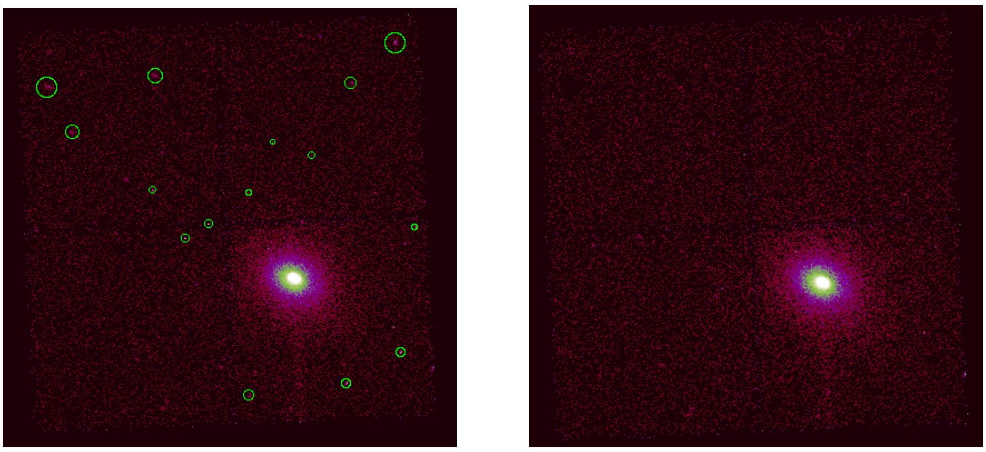

Figure 5.3: Images of X-ray surface brightness of RXC J1504.1-0248 cluster. Left image shows the selected regions (small circles) as point sources before being excluded and single marked region for including in the analysis. The right image is after all the point sources are being removed.

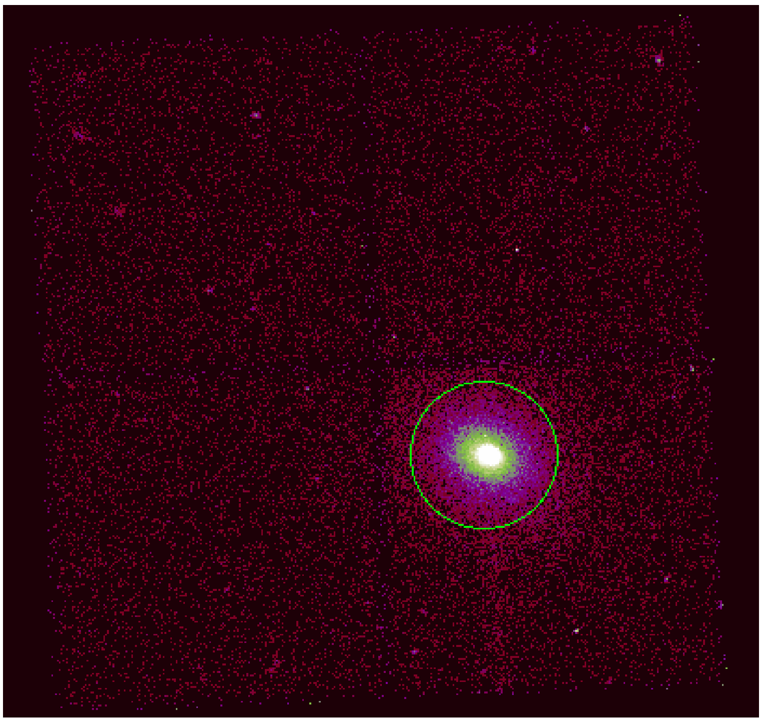

Figure 5.4: Creating a region for the galaxy cluster for excluding from "deflaring" process.

The quantum efficiency multiplied by the effective detector area for each event is encoded in the supplementary response files[38]. This is required to extrapolate what a perfect detector would act like from the data collected. To crop the area of

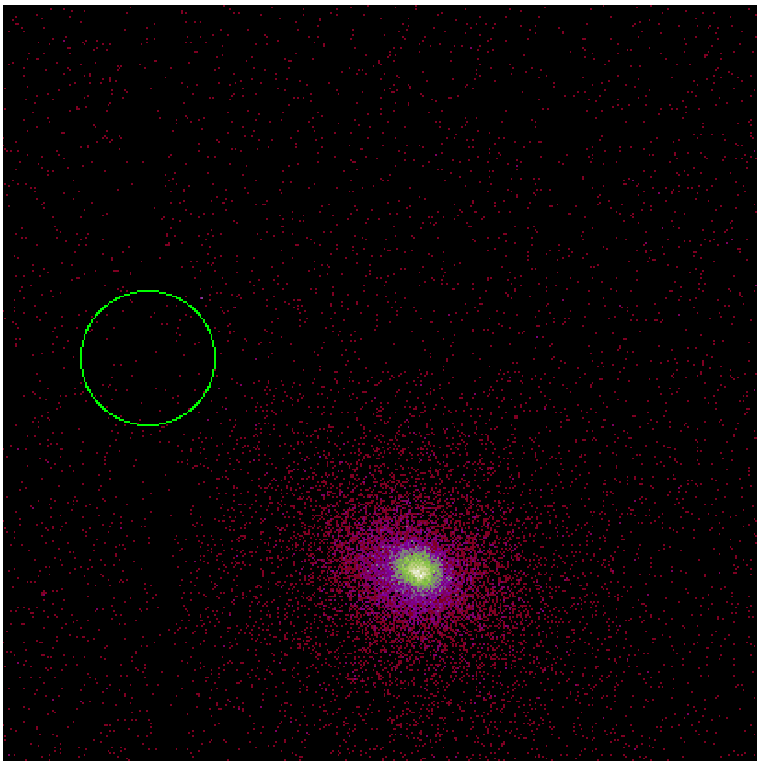

Figure 5.5: By producing ARF and RMF files from the accumulating parts of each of the ACIS-I CCDs, we can interpolate how an ideal detector might observe relying on what has been genuinely observed.

of our interest we need to draw a box region to generate the density and pressure maps. The $0 \cdot 7 - 8$ keV range provides the optimum quantum efficiency and effective area. ClusterPyXT uses this range for filtering observations and backgrounds by default. To such an extent, this value is recommended for all cluster analysis and we are also keeping the default value. To complete this step, we opened our *rxc48 xray surface brightness nosrc.fits* file and cropped the region and saved it as *acisI region 0.reg*, which is shown as a green box in the *rxc48 xray surface brightness nosrc.* file shown in fig 5.6 .

For spectral fitting, ClusterPyXT uses Adaptive Circular Binning algorithm or ACB. There are two other widely used binning algorithms named as weighted Voronoi Tessellation (WVT) and Contour Binning. The reason behind using ACB instead of WVT and Contour Binning are as follows as:

- The resolution of WVT and contour binned maps are lower[38].
- WVT and contour binned maps both on the assumption that temperature characteristics correlate to surface brightness characteristics, which is not necessarily true.

Data binning produces following data:

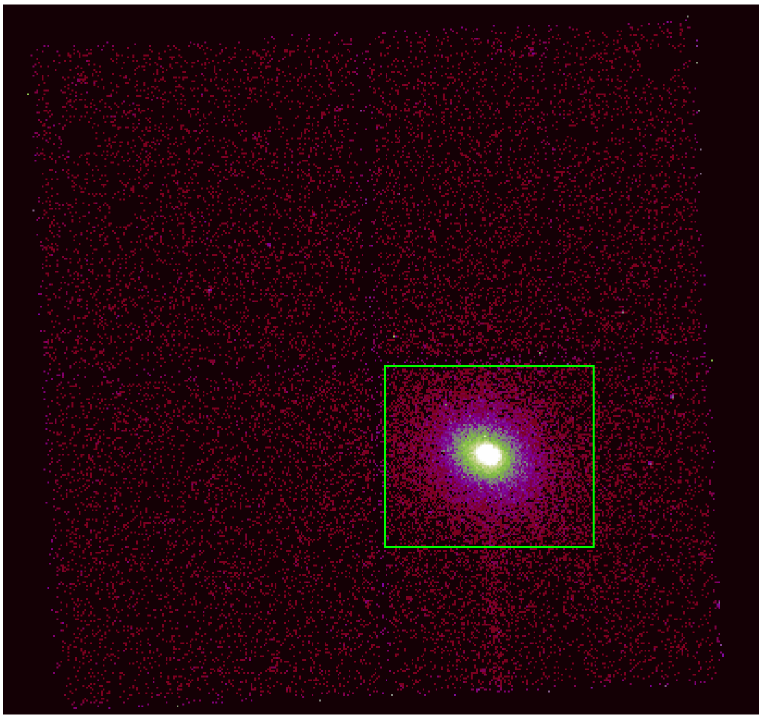

Figure 5.6: Cropping the region from X-ray surface brightness map for generating temperature, density and pressure maps.

- draws scale-map
- computes efficient time limits
- Is used to generate the zones on every spectral fit
- provides the scripts that are required for the spectral fittings

Sherpa tool is used for the spectral fitting procedure. There are a total 971 iterations in our spectral fittings and 23266 regions. As discussed in 3.6 the process can be run in three different resolutions which controls how many pixels have spectral fits completed. We used high resolution settings for our spectral fittings. After applying spectral fittings in the cropped region shown in figure 5 density map and brightness map is generated. The density map is shown in figure 5.7.

5.4 Cold front detection

After brightness and density maps are generated, it is ready to detect drops. We wrote a python script for this. Which is available in this GitHub link:
https://github.com/ZareefJafar/MapToProfile.git Both the brightness and density maps are in Flexible Image Transport System or shortly fits the format which is discussed in chapter $4 \cdot 2$. The pseudocode of this algorithm is shown in figure 5.8. We retrieved the units, pixel value, dimensions and other parameters from the header extension of the fits file of density and brightness map.The header contains keyword value statements which define the HdU data organization and the information format[24] (see figure 5.9)

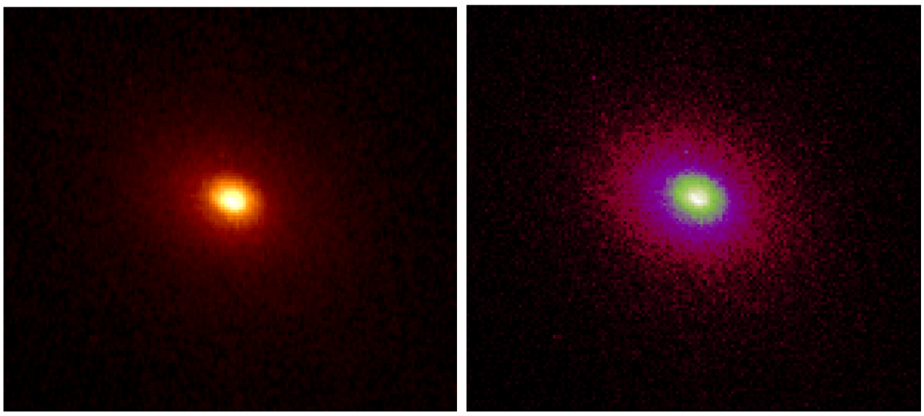

Figure 5.7: Generated brightness and density map after spectral fittings of RXC J1504.1-0248 cluster.

```
Function MapToProfile(fits)
1.  st_radi:    INPUT start position angle from user
2.  en_radi:    INPUT end position angle from user
3.  img:    READ fits data unit
4.  hd: READ fits header unit
5.  arg_max:    DETERMINE pixel with highest energy value
6.  center: SET index of highest  value pixel as index of center
7.  cen_x, cen_y:   INIT x and y coordinate of center index separately
8.  img_x,img_y:    GET number of pixel from image in x and y coordinate
9.  dis_x, dis_y:   INIT 2d mesh with each cell containing number of
                    pixel distance from the center
10. tan:    Compute tangent of each point with respect to center (radian angle)
11. rad:    INIT a list of radial distance  from 0 to max pixel distance set by user
12. reg:    INIT a 2D mesh with with True label for cells between
            start position angle and end position angle
13. crop_img:   reg * img
14. en: empty list with a length of rad for storing energy value of each pixel
15. index:  INIT index equal to 0
16. bin_size:   set bin size to 0
17. FOR radius in a rad
18.     mask:   select pixels of radius
19.     values: take values of mask pixels
20.     SET intensity of the index as mean of values
21.     INCREMENT index
22. deg:    take absolute value of CDELT1 or size of each pixel
23. dis:    Convert each radius to kiloparsec as 1/((rad*deg)*3600)
24. profile:    plot distance(dis) vs energy(en)
```

Figure 5.8: Algorithm for generating density and brightness profile from density and brightness maps.

```
SIMPLE  =                    T / file does conform to FITS standard
BITPIX  =                  -64 / number of bits per data pixel
NAXIS   =                    2 / number of data axes
NAXIS1  =                  148 / length of data axis
NAXIS2  =                  132 / length of data axis
EXTEND  =                    T / FITS dataset may contain extensions
COMMENT   FITS (Flexible Image Transport System) format is defined in 'Astronomy
COMMENT   and Astrophysics', volume 376, page 359; bibcode: 2001A&A...376..359H
HDUNAME = 'rxc_temp_density.fits' / ASCDM block name
ORIGIN  = 'ASC     '           / Source of FITS file
CREATOR = 'reproject_image - Version CIAO 4.13' / tool that created this output
ASCDSVER= 'CIAO 4.13'          / ASCDS version number
ASOLFILE= 'pcadf05793_000N001_asol1.fits'
THRFILE = 'acisD1996-11-01evtspltN0002.fits'
TLMVER  = 'P014    '           / Telemetry revision number (IP&CL)
REVISION=                    4 / Processing version of data
CHECKSUM= 'COOHFLLFCLLFCLLF'   / HDU checksum updated 2021-05-22T21:37:12
DATASUM = '744515460'          / data unit checksum updated 2021-05-22T21:37:12
CONTENT = 'EVT1    '           / What data product
HDUSPEC = 'ACIS Telemetry Products: Level 0 to ASC Archive ICD Rev 2.11' / ICD r
HDUDOC  = 'ASC-FITS-2.0: McDowell, Rots: ASC FITS File Designers Guide'
HDUVERS = '1.0.0   '
HDUCLASS= 'OGIP    '
HDUCLAS1= 'EVENTS  '
HDUCLAS2= 'ALL     '
PIX_ADJ = 'EDSER   '           / Subpixel adjustment algorithm
RAND_SKY=  0.0000000000000E+00
SUBPIXFL= 'acisD1999-07-22subpixN0001.fits'
RAND_PI =  1.0000000000000E+00
```

Figure 5.9: RXC J1504.1-0248 density map header unit.

We made a custom python script that reads density and brightness maps of galaxy clusters and creates a distance vs average energy graph to observe the increase or decrease of density or brightness in respect to distance from the center. To compare our result, we showed the brightness and density profile of the same cluster[32].The author of this paper showed the profile from a particular annulus of brightness and density map. Yet, to make things simpler we made our profile from the center (brightest) to the maximum radius of the map. In figure 5.8 the two annuli of RXC J1504.1-0248 - are shown from two different position angles retrieved from [32]. The position angle of the North-West anulus is 2 to 80 degrees and for the South-East it is 180 to 280.

In figure $5 \cdot 11$ we compared our brightness profiles with the same profiles from [32]. According to the author the jump radius from the center for the North-West cold front is at $59 \cdot 2(\pm^{5\cdot3}_{0\cdot11})$ and for South-East it is $46 \cdot 8(\pm^{8}_{1})$. In our result it is $58(\pm3)$ North-West and $45(\pm5)$ for South-East.

In figure $5 \cdot 12$ we compared our density profiles with the same profiles from [32]. According to the author of this paper the jump radius from center for North-West cold front is at $59 \cdot 2(\pm^{5\cdot3}_{0\cdot11})$ and for South-East it is $46 \cdot 8(\pm^{8}_{1})$. In our result it is $58(\pm3)$ North-West and $45(\pm5)$ for South-East.

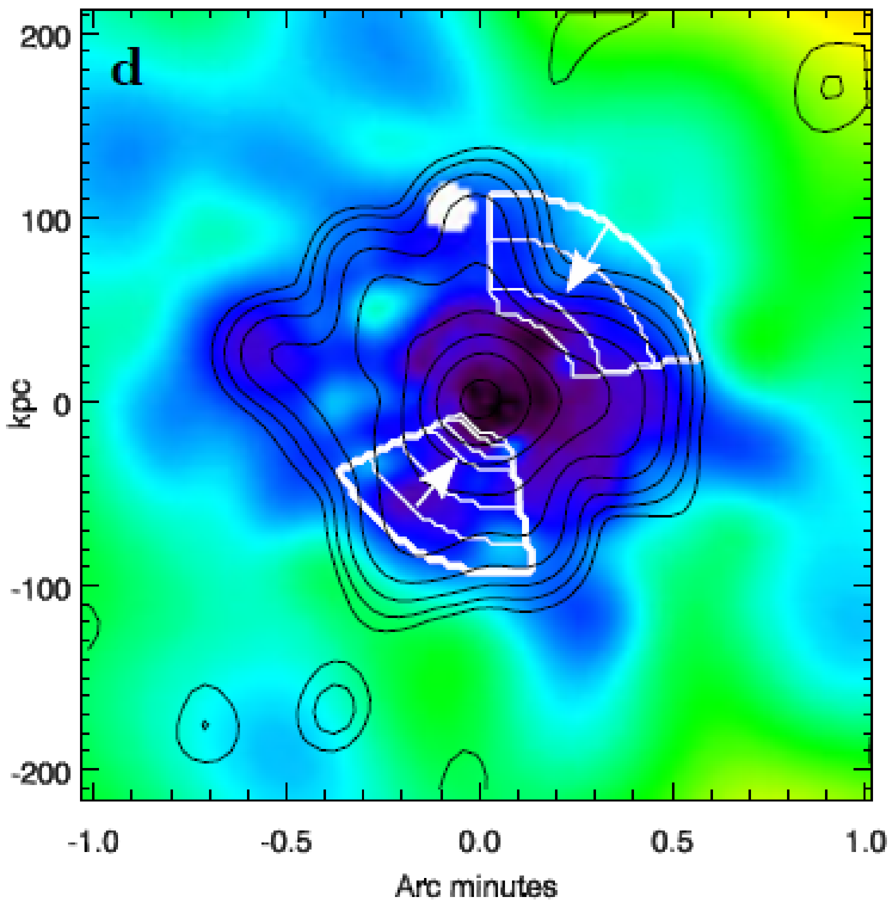

Figure 5.10: The white sector annuli on the temperature map indicate the sectors from which the brightness and density profiles were extracted. The arrows indicate the CFs' locations.

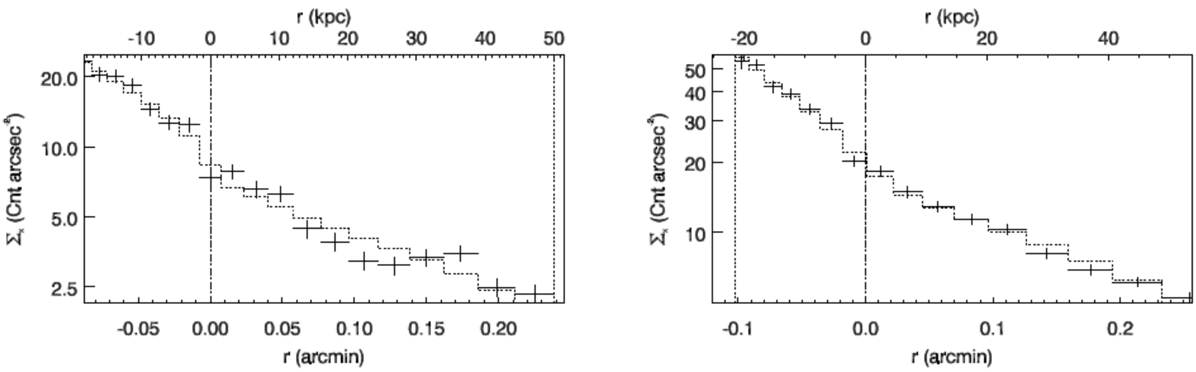

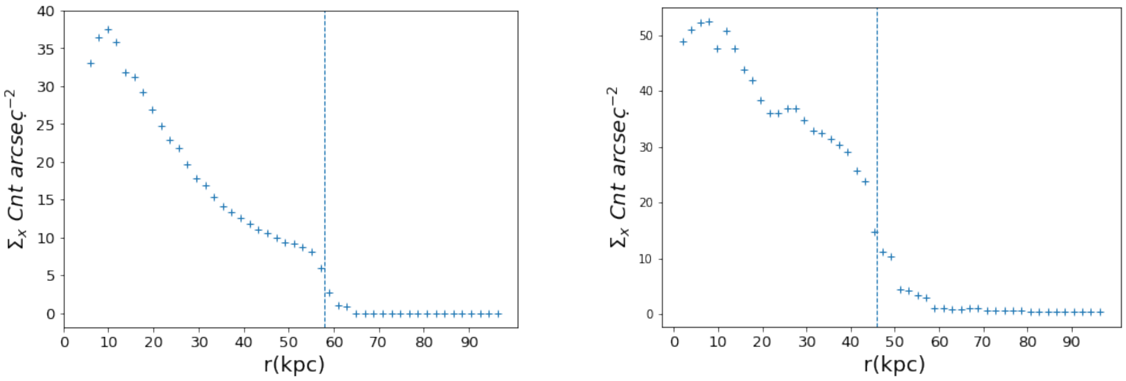

Figure 5.11: Comparison between the brightness profile of [32]and our derived brightness profile for cold front detection of RXC J1504.1-0248. The left and right columns represent the cluster's north-east and south-west cold fronts, respectively. The top and bottom Profiles correspond to the colds front from [32] and our derived cold fronts respectively. The dotted lines indicate the estimate location of cold fronts.

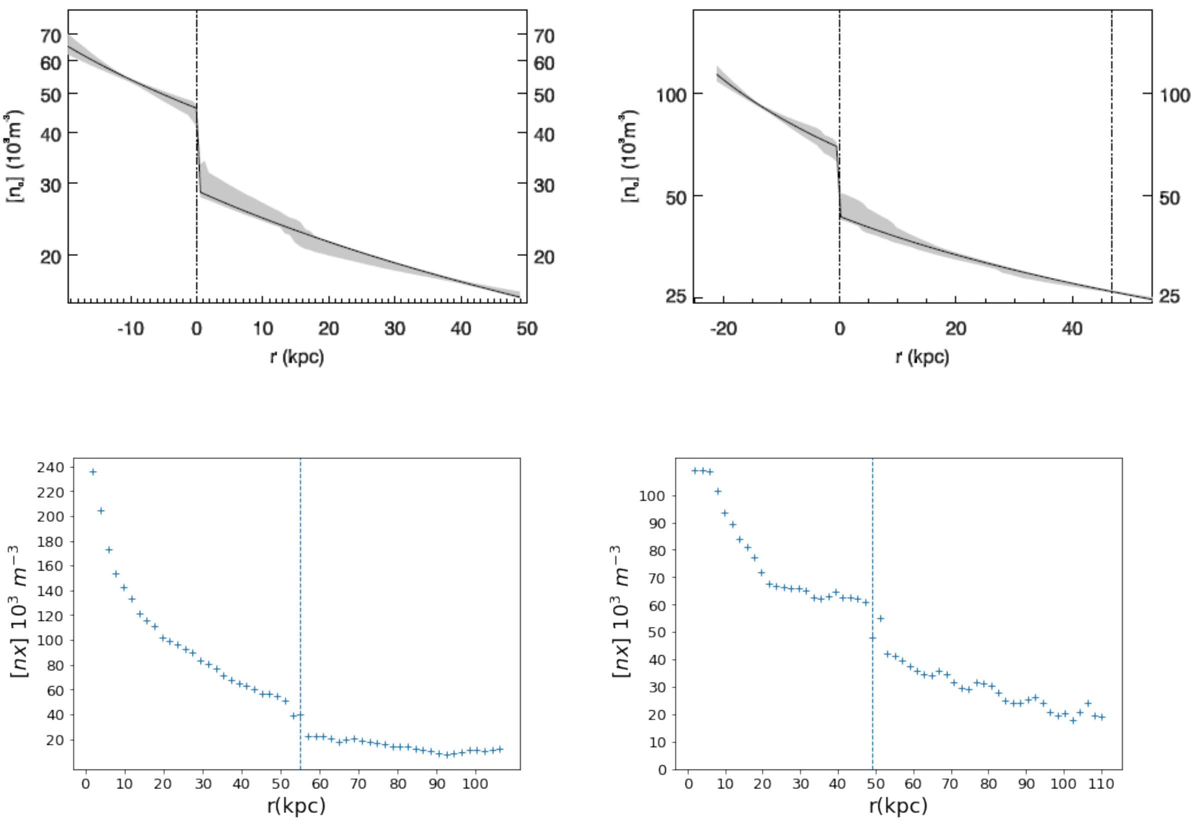

Figure 5.12: Comparison between the density profile of[32] and our derived density profile for cold front detection of RXC J1504.1-0248 The profiles in the left and right columns correspond to the cluster's north-east and south-west cold fronts, respectively. The top and bottom Profiles correspond to the colds front from [32] and our derived cold fronts respectively. The dotted lines indicate the estimate location of cold fronts.

Galaxy clusters	Cold fronts	Position angles(degree)	Jumpradii(rj) (kpc) From [32]	Jump radii(rj)(kpc) From our analysis
RXC J1504.1-0248	North-West	2-80	$59 \cdot 2(\pm^{5\cdot3}_{0\cdot11})$	58(±3)
RXC J1504.1-0248	South-East	180-280	$46.8(\pm^{8}_{1})$	45(±5)

Table 5.1: Parameters of the Cold Fronts in the targeted clusters

5.5 Result analysis:

As we can see in Table 1 from the same position angle of North-West and South-East cold fronts the jump radius is almost identical in our experiment and result of [32]. There is some accuracy in our jump radius because of some limitations in X-ray peak calculation in our algorithm which selects the pixel with highest density or brightness value as the center. In some galaxy clusters we tested the pixel with the highest X-ray emission can be a little bit outside from the X-ray dense center of the galaxy cluster. Which also happened to galaxy cluster RXC J1504.1-0248 and we had to manually fix this issue which is not convenient. This is one of the limitations of our method.
The reason behind choosing the RXC J1504.1-0248 galaxy cluster is because of its significant density and brightness drop. In the result of [32] the author de-noised in the scale-map by means of MSVST + curvelet analysis. For this reason, it's brightness and density profile are illustrated so clearly. In our case because of the resolution limitation and no MSVST + curvelet analysis the profiles are not clear. But the drop is significant enough to know the cold-front location and we can estimate the range easily. If you compare the profiles of the author and ours the jump radius range overlaps more than 90%.

Chapter 6

6.1 Future Work

There is a lot of scope of improvement in our work. There are some limitations in ClusterPyXT for generating temperature and pressure maps. If we are able to merge the temperature and pressure profile with our density and brightness profile it will help to provide more solid proof of the existence of mini halo as well as its location. In future, we will try to integrate some features of another pipeline developed by Jean-Paul Breuer which generates maps in a more controlled way which uses statistically independent bins for binning. Hopefully, we will start to make our own pipeline specifically designed for detecting cold fronts in any potential cluster. This will not only be helpful for minihalo detection but also detecting halos. Merging these results of X-ray observation with radio observation may help to understand the existence of these objects more deeply. Though it is not possible to process radio observations of galaxy clusters in normal desktop computers, the end result of radio observation can be overlaid in X-ray maps for studying the other characteristics of minihalo which is not possible only with X-ray observation. Some new research is undergoing with meerkat and LOFAR observatories for radio observation. Hopefully in future these data will be publicly available.

6.2 Conclusion

In our paper we developed an X-ray data analysis workflow with a combination of different open source software packages, tools and our own python script to detect the location of mini-halo in potential galaxy clusters. In the heart of our system is the CIAO environment developed by the Chandra X-Ray Center alone. We showed how ClusterPyXT software python pipeline automated different CIAO commands for generating X-ray surface brightness and density maps from our sample X-ray observations of a galaxy cluster with the help of adaptive binning algorithm. In the end we implemented our own python script to process those maps for generating the ultimate result which is a brightness and a density profile proving the existence of mini-halo in that particular galaxy-cluster. We also gave detailed instructions for selecting different parameters for different stages of processing. We compared our output with a similar research paper by **asad**. For this we have chosen the RXC J1504.1-0248 galaxy cluster and all of our data analysis is done on the X-ray ray of this particular galaxy cluster. Our main goal is to develop a complete system which can be used to detect mini-halo and hopefully halo relics from galaxy clusters which may help beginners in the field of data driven astronomy. Moreover,learners can edit these scripts to generate customized results which may unveil some hidden phenomena which has never been seen before.

Bibliography

[1] F. Zwicky, "The redshift of extragalactic nebulae," *Helvetica Physica Acta*, vol. 6, pp. 110–127, 1933.

[2] ——, "The redshift of extragalactic nebulae," *Helvetica Physica Acta*, vol. 6, pp. 110–127, 1933.

[3] ——, "On the masses of nebulae and of clusters of nebulae," *The Astrophysical Journal*, vol. 86, p. 217, 1937.

[4] T. Bohuski, R. Dufour, and D. Osterbrock, "Nebular photometry with an echelle spectrometer:[o iii] line ratios in ngc 1976 and ngc 6853.," *The Astrophysical Journal*, vol. 188, pp. 529–532, 1974.

[5] E. Kellogg, J. Baldwin, and D. Koch, "Studies of cluster x-ray sources, energy spectra for the perseus, virgo, and coma clusters," *The Astrophysical Journal*, vol. 199, pp. 299–306, 1975.

[6] A. Cavaliere and R. Fusco-Femiano, "X-rays from hot plasma in clusters of galaxies," *Astronomy and Astrophysics*, vol. 49, pp. 137–144, 1976.

[7] L. Pekurovskii, "Shock wave diffraction on a thin wedge moving with a slip relative to the wave front with irregular shock interaction," *Journal of Applied Mathematics and Mechanics*, vol. 44, no. 2, pp. 183–190, 1980.

[8] C. L. Sarazin, "X-ray emission from clusters of galaxies," *Reviews of Modern Physics*, vol. 58, no. 1, p. 1, 1986.

[9] R. Winglee, "Particle/fluid simulations of an eruptive flare: Identifying the field-aligned currents responsible for the hard x-rays," *Solar Physics*, vol. 154, no. 1, pp. 123–156, 1994.

[10] S. A. Shectman, S. D. Landy, A. Oemler, D. L. Tucker, H. Lin, R. P. Kirshner, and P. L. Schechter, "The las campanas redshift survey," *arXiv preprint astro-ph/9604167*, 1996.

[11] J. F. Navarro, C. S. Frenk, and S. D. White, "A universal density profile from hierarchical clustering," *The Astrophysical Journal*, vol. 490, no. 2, p. 493, 1997.

[12] B. Wilkes, "Ciao 1.0 to ciao 4.11: A world apart," 1999.

[13] J. J. Drake and B. J. Wargelin, "Instruments: Letg," *Chandra News*, vol. 8, p. 7, 2001.

[14] M. Markevitch, A. Vikhlinin, and P. Mazzotta, "Nonhydrostatic gas in the core of the relaxed galaxy cluster a1795," *The Astrophysical Journal Letters*, vol. 562, no. 2, p. L153, 2001.

[15] P. Mazzotta, M. Markevitch, W. Forman, C. Jones, A. Vikhlinin, and L. VanSpeybroeck, "Chandra observation of ms 1455.0+ 2232: Cold fronts in a massive cooling flow cluster?" *arXiv preprint astro-ph/0108476*, 2001.

[16] P. M. Ricker and C. L. Sarazin, "Off-axis cluster mergers: Effects of a strongly peaked dark matter profile," *The Astrophysical Journal*, vol. 561, no. 2, p. 621, 2001.

[17] M. Corso, W. Auwarter, M. Muntwiler, A. Tamai, T. Greber, and J. Osterwalder, "Nanomesh: Self organisation of boron nitride on rh (111)," in *APS March Meeting Abstracts*, vol. 2004, 2004, pp. V32–001.

[18] P. Mazzotta, E. Rasia, L. Moscardini, and G. Tormen, "Comparing the temperatures of galaxy clusters from hydrodynamical n-body simulations to chandra and xmm–newton observations," *Monthly Notices of the Royal Astronomical Society*, vol. 354, no. 1, pp. 10–24, 2004.

[19] P. M. Kalberla, W. Burton, D. Hartmann, E. M. Arnal, E. Bajaja, R. Morras, and W. Pöppel, "The leiden/argentine/bonn (lab) survey of galactic hi-final data release of the combined lds and iar surveys with improved stray-radiation corrections," *Astronomy & Astrophysics*, vol. 440, no. 2, pp. 775–782, 2005.

[20] Y. Ascasibar and M. Markevitch, "The origin of cold fronts in the cores of relaxed galaxy clusters," *The Astrophysical Journal*, vol. 650, no. 1, p. 102, 2006.

[21] A. Carballido, S. Fromang, and J. Papaloizou, "Mid-plane sedimentation of large solid bodies in turbulent protoplanetary discs," *Monthly Notices of the Royal Astronomical Society*, vol. 373, no. 4, pp. 1633–1640, 2006.

[22] A. Fruscione, J. C. McDowell, G. E. Allen, N. S. Brickhouse, D. J. Burke, J. E. Davis, N. Durham, M. Elvis, E. C. Galle, D. E. Harris, *et al.*, "Ciao: Chandra's data analysis system," in *Observatory Operations: Strategies, Processes, and Systems*, International Society for Optics and Photonics, vol. 6270, 2006, p. 62701V.

[23] J. R. Peterson and A. C. Fabian, "X-ray spectroscopy of cooling clusters," *Physics reports*, vol. 427, no. 1, pp. 1–39, 2006.

[24] J. Carter and A. Read, "The xmm-newton epic background and the production of background blank sky event files," *Astronomy & Astrophysics*, vol. 464, no. 3, pp. 1155–1166, 2007.

[25] G. Hussain, M. Jardine, J.-F. Donati, N. Brickhouse, N. Dunstone, K. Wood, A. Dupree, A. Collier Cameron, and F. Favata, "The coronal structure of ab doradus determined from contemporaneous doppler imaging and x-ray spectroscopy," *Monthly Notices of the Royal Astronomical Society*, vol. 377, no. 4, pp. 1488–1502, 2007.

[26] M. Markevitch and A. Vikhlinin, "Shocks and cold fronts in galaxy clusters," *Physics Reports*, vol. 443, no. 1, pp. 1–53, 2007.

[27] R. Thomson, "The qualitative longitudinal case history: Practical, methodological and ethical reflections," *Social Policy and Society*, vol. 6, no. 4, pp. 571–582, 2007.

[28] E. Dwek and F. Galliano, "The evolution of pahs and sn-condensed dust in galaxies," *The Evolving ISM in the Milky Way and Nearby Galaxies*, p. 5, 2009.

[29] S. K. Sharma, P. K. Tyagi, A. K. Upadhyay, M. A. Haque, S. S. Mohanty, K. Raghavendra, and A. P. Dash, "Efficacy of permethrin treated long-lasting insecticidal nets on malaria transmission and observations on the perceived side effects, collateral benefits and human safety in a hyperendemic tribal area of orissa, india," *Acta tropica*, vol. 112, no. 2, pp. 181–187, 2009.

[30] H. Böhringer and N. Werner, "X-ray spectroscopy of galaxy clusters: Studying astrophysical processes in the largest celestial laboratories," *The Astronomy and Astrophysics Review*, vol. 18, no. 1-2, pp. 127–196, 2010.

[31] D. P. Huenemoerder, A. Mitschang, D. Dewey, M. A. Nowak, N. S. Schulz, J. S. Nichols, J. E. Davis, J. C. Houck, H. L. Marshall, M. S. Noble, *et al.*, "Tgcat*: The chandra transmission grating data catalog and archive," *The Astronomical Journal*, vol. 141, no. 4, p. 129, 2011.

[32] D. G. d. G. Khan Muhammad Bin Asad, "Studio della formazione dei cold fronts e dei mini aloni radio indotta dall'oscillazione del gas intergalattico nel centro degli ammassi di galassie(study of the formation of cold fronts and radio mini-halos induced by the intergalactic gas sloshing in the cores of galaxy clusters)," 2011.

[33] V. Tangri and N. Chande, "Quality of internet-based information on gastrointestinal diseases," *Canadian Journal of Gastroenterology*, vol. 25, no. 2, pp. 93–96, 2011.

[34] M. Gitti, F. Brighenti, and B. R. McNamara, "Evidence for agn feedback in galaxy clusters and groups," *Advances in Astronomy*, vol. 2012, 2012.

[35] J. H. Kim, S. Peirani, S. Kim, H. B. Ann, S.-H. An, and S.-J. Yoon, "Formation of warped disks by galactic flyby encounters. i. stellar disks," *The Astrophysical Journal*, vol. 789, no. 1, p. 90, 2014.

[36] D. Vrandečić and M. Krötzsch, "Wikidata: A free collaborative knowledgebase," *Communications of the ACM*, vol. 57, no. 10, pp. 78–85, 2014.

[37] ——, "Wikidata: A free collaborative knowledgebase," *Communications of the ACM*, vol. 57, no. 10, pp. 78–85, 2014.

[38] B. Alden, E. J. Hallman, D. Rapetti, J. O. Burns, and A. Datta, "The galaxy cluster 'pypeline'for x-ray temperature maps: Clusterpyxt," *Astronomy and Computing*, vol. 27, pp. 147–155, 2019.

[39] S. Giacintucci, M. Markevitch, R. Cassano, T. Venturi, T. E. Clarke, R. Kale, and V. Cuciti, "Expanding the sample of radio minihalos in galaxy clusters," *The Astrophysical Journal*, vol. 880, no. 2, p. 70, 2019.

[40] M. Tremmel, T. R. Quinn, A. Ricarte, A. Babul, U. Chadayammuri, P. Natarajan, D. Nagai, A. Pontzen, and M. Volonteri, "Introducing romulusc: A cosmological simulation of a galaxy cluster with an unprecedented resolution," *Monthly Notices of the Royal Astronomical Society*, vol. 483, no. 3, pp. 3336–3362, 2019.

[41] A. Janzadeh and M. Zandieh, “Design feasibility of a net-zero energy neighborhood in qazvin,” *Energy Efficiency*, vol. 14, no. 1, pp. 1–21, 2021.

[42] M. E. De los Rıos, “Métodos de aprendizaje automático aplicados a problemas cosmológicos,”